# Modeling and numerical investigation of the performance of gas diffusion electrodes for the electrochemical reduction of carbon dioxide to methanol

| | |
|---|---|
| Journal: | *Industrial & Engineering Chemistry Research* |
| Manuscript ID | ie-2020-02358q |
| Manuscript Type: | Article |
| Date Submitted by the Author: | 09-May-2020 |
| Complete List of Authors: | El-Shafie, Omnia; Cairo University Faculty of Engineering, Chemical Engineering Department<br>El-Maghraby, Rehab; Suez University, Faculty of Petroleum and Mining Engineering, Petroleum Refinery and Petrochemical Engineering Department; Suez University, cOil and Green Chemistry Research Centre / Enhanced Oil Recovery Laboratory<br>Albo, Jonathan; Universidad de Cantabria, Chemical and Biomolecular Engineering<br>Fateen , Seif-Eddeen ; Zewail City of Science and Technology, Environmental Engineering Program; Cairo University Faculty of Engineering, Chemical Engineering Department<br>Abdelghany, Amr; Cairo University Faculty of Engineering, Chemical Engineering Department |
| | |

SCHOLARONE™
Manuscripts

# Modeling and numerical investigation of the performance of gas diffusion electrodes  for the electrochemical reduction of carbon dioxide to methanol

Omnia A. El-Shafie *[a], Rehab M. El-Maghraby [b,c], Jonathan Albo [d], Seif-Eddeen K.

Fateen [a,e] and Amr Abdelghany [a].


[a]Chemical Engineering Department, Faculty of Engineering, Cairo University, 12613

Giza, Egypt E-mail: omniaelshafie737@gmail.com


[b]Petroleum Refinery and Petrochemical Engineering Department, Faculty of Petroleum

and Mining Engineering, Suez University, Suez, Egypt


[c]Oil and Green Chemistry Research Centre / Enhanced Oil Recovery Laboratory, Suez

University, Suez, Egypt

[d]Department of Chemical & Biomolecular Engineering, University of Cantabria, 39005

Santander, Spain

[e]Environmental Engineering Program, Zewail City of Science and Technology, 12588

Giza, Egypt

## ABSTRACT

In this study, a model was built to investigate the role of $Cu_2O$-ZnO based gas diffusion

electrodes in enhancing the reduction of carbon dioxide into methanol inside an

electrochemical cell. The model was simulated using COMSOL Multiphysics software and

validated using experimental results.  It showed reasonable agreement with an average

error of 6%. The model demonstrated the dependence of methanol production rate and

faradaic efficiency on process key variables; current density (j = 5-10 mA/cm$^2$), gas flow

rate ($Q_g/A$ = 10-20 ml/min cm$^2$), electrolyte flow rate and $CO_2$ gas feed concentration. The

results showed a maximum methanol production rate of 50 µmol/m$^2$ s, and faradaic

efficiency of 56 % at −1.38 V vs. Ag/AgCl. From the economic point of view, it is

recommended to use a gas stream of 90% or slightly lower $CO_2$ concentration and an

electrolyte flow rate as low as 2 ml/min cm$^2$.

## 1.    Introduction

Anthropogenic carbon dioxide ($CO_2$) emissions to the atmosphere are reaching an alerting level.[1] Rapid actions need to be implemented in order to limit such increase and find alternative routes to utilize $CO_2$.[2] $CO_2$ valorization is taking more interest nowadays as a way through which captured $CO_2$ is utilized to more valuable products and chemicals. The electrochemical reduction of $CO_2$ has been proposed as a potential option for $CO_2$ valorization. Through this simple electrochemical reduction process, a carbon-neutral energy route will be established where $CO_2$ could be converted to synthesis gas, formaldehyde, different types of alcohols and other valuable products. Despite being a simple process of high potentials[1,3–7], some challenges[1,3,8,9] are hindering its industrial application. One of those challenges is the low $CO_2$ solubility in aqueous solution (0.033 mol/l at STP)[3], that affects the mass-transfer of $CO_2$ into the aqueous phase and limits the selectivity at high current densities. Some techniques[3] were proposed to overcome such limitations, which include; lowering the operating temperature[10], increasing the $CO_2$ partial pressure[11,12] and using non-aqueous solutions[13] or solid polymer electrolytes (SPE)[14–16]. The most promising option to overcome such mass transfer limitations is to

use gas diffusion electrodes (GDEs)[17–20] where the reacting $CO_2$ could be introduced to

the cell directly in the gas phase, resulting in an improvement in the cell performance.

The gas diffusion electrode consists of two layers; the gas diffusion layer (GDL),

referred to as diffusion medium, and the catalyst layer (CL).[21] The GDL is usually placed

between the CL and the gas channel, and is typically made from carbon-based materials[22]

to maintain high electric conductivity, gas permeability, and stability over a wide potential

range.[22] The GDL is in direct contact with the gas channel where it acts as a gas

distributor and current collector. In most cases, the GDL is of a hydrophobic nature to

prevent water flooding through the electrode which facilitates reactant gas transportation

to the CL.[21] The GDE improves the electrochemical cell performance by enhancing the

catalyst stability, it provides the necessary mechanical support and conducts electrons

through its solid phase at low resistance. According to the literature [23–25], the main

advantage of the GDE is the ability to provide a three-phase interface between the solid

catalyst particles, the gaseous reacting $CO_2$, and the liquid electrolyte solution. This will

increase the active surface area of the electrocatalyst available for the reduction reaction.

Despite that the exact pathway for the electrochemical reduction of $CO_2$ in a three-phase

interface medium is still unknown[26], it is hypothesized that only gaseous $CO_2$ is involved in the reduction reaction[23–25]. However, other researchers, for example, Weng et al.[18] opposed this hypothesis and believe that $CO_2$ needs to dissolve first in the aqueous solution for the reduction reaction to occur. Still more investigation is needed, so, in the present study, the nature of the reduction reaction is looked at.

Many experimental studies on the electrochemical reduction of $CO_2$ to carbon monoxide (CO)[27,28] and formic acid[28–30] could be found in literature. However, limited experimental data is available on the electrochemical conversion of $CO_2$ to alcohol[6,31–37]. The compilation of experimental data and integration with modeling studies is an essential step in order to facilitate the upscaling of the electrochemical reduction of $CO_2$ into the industrial scale. According to the literature, and as far as the authors know, only one study, conducted by Yosra et. al., 2017[38] investigated the electrochemical reduction of $CO_2$ to methanol ($CH_3OH$). Yosra et. al., 2017[38] developed a mathematical model for the reduction of $CO_2$ into $CH_3OH$ by using a planner type $Cu_2O/ZnO$-based electrode in an aqueous solution of $KHCO_3$. No GDE was used in this study or other studies to model the conversion of $CO_2$ into $CH_3OH$. However, the work of Yosra et. al., 2017[38] has paved the

way for further developments in the modeling of the electrochemical cell to convert $CO_2$ into $CH_3OH$. The current study is considered an advanced step towards the introduction of the GDE in the electrochemical reduction of $CO_2$ to $CH_3OH$ and ethanol ($C_2H_5OH$). Modeling GDE in the electrochemical conversion of $CO_2$ to different products was investigated by a limited number of researchers. This was listed in Table 1 and compared to the present study.

Table 1. Comparison of literature modeling studies done for $CO_2$ electrochemical reduction on GDE-based electrodes

| Reference | Cathodic Catalyst | Main Product | Model Dimensions | CL modeled as | Acid-base Reactions | Phase Flow |
|---|---|---|---|---|---|---|
| Wu et. al.[24] | Pt | CO | 2D | Interface | N.C | Single |
| Georgopoulou et. al.[39] | Sn | Formate | 2D | Interface | C | Two |
| Weng et. al.[18] | Ag | CO | 1D | Domain | C | Single |
| Present model | $Cu_2O$-ZnO | $CH_3OH$ | 2D | Domain | C | Single |

where N.C: Not considered; C: Considered

Wu et. al., 2015[24] developed a model for the production of CO using Pt-based GDE. In their study, they investigated the operating and design parameters effect on process

performance. However, in the modeled electrochemical cell the produced CO exits the

gas channel together with the unreacted $CO_2$, hence, the probability of CO interrupting

the electrolyte flow (i.e., leading to a two-phase flow) is low. In addition, their model

neglected the acid-base reactions occurring inside the electrolyte although such reactions

affect the reacting $CO_2$ concentration and its solubility in the electrolyte.

Georgopoulou et. al., 2016[39] developed a model for the electrochemical reduction of

$CO_2$ into formic acid using GDE. As the case with Wu et. al.,2015[24], in their model the

products exit the gas channel together with the unreacted $CO_2$ while the formic acid is

produced in the aqueous phase, thus their model is considered a two-phase flow. On the

other hand, Weng et al.,2019 [18] treated the CL in their model, to produce CO, as a domain

not as an interface like other researchers.[24,39] Also, they introduced the concept of ideal

saturated CL to their model, which refers to the fraction of the catalyst pore volume

occupied by liquid electrolyte. According to the literature, no work was conducted to

investigate the GDE in the electrochemical reduction of $CO_2$ into $CH_3OH$, so, more work

is needed.

In this study, a mathematical model was developed and validated for the continuous electrochemical reduction of $CO_2$ to $CH_3OH$; using GDE, given the high demand and the importance of $CH_3OH$ and $C_2H_5OH$ for many chemical and petrochemical industries[6,7]. This work presents a 2D (two-dimensional), steady-state, isothermal model for a continuous filter-press electrochemical cell. The model was simulated using the commercial software COMSOL V5.2. Modified forms of Butler-Volmer equations have been used for expressing the process kinetics. In many cases in the literature, the exchange current density; representing current at thermodynamic equilibrium, is taken as a constant value for each specific reaction and calculated as a fitting parameter, despite being dependant on process conditions, catalyst structure, and particle size.[3,40] In this work, the exchange current density was related to the flow rates and applied current density through an empirical equation. This model focuses on the mathematical relations describing the effect of using the GDEs to overcome the $CO_2$ mass transfer limits and to increase the production rate. To achieve this goal, the model incorporated charge, mass and momentum transport with electrode kinetics.

## 2.    Experimental Equipment and Conditions

### 2.1.    Materials and Equipment

The $Cu_2O$/ZnO-based GDEs were prepared according to a procedure previously reported.[32,33] $Cu_2O$ (Sigma Aldrich, particle size <5 μm, 97% purity) and ZnO particles (ACROS organic, <45 μm, 99.5%) were mixed with a Nafion® dispersion 5 wt.% (Alfa Aesar) and isopropanol (IPA) (Sigma Aldrich), with a 70/30 catalyst/Nafion mass ratio and a 3% solids (catalyst + Nafion). The prepared $Cu_2O$/ZnO inks were airbrushed onto carbon papers (TGP-H-60, Toray Inc.) and then, rinsed with deionized water and dried at ambient temperature before use. The catalyst loading was kept at 1mg $cm^{-2}$ of $Cu_2O$ and 1 mg $cm^{-2}$ of ZnO.

### 2.2.    Methodology

1
2
3
4
5
6
7
8
9
10
11
12
13
14
15
16
17
18
19
20
21
22
23
24
25
26
27
28
29
30
31
32
33
34
35
36
37
38
39
40
41
42
43
44
45
46
47
48
49
50
51
52
53
54
55
56
57
58
59
60

The experimental setup components, shown in Fig. 1.a is fully detailed in the works of

Albo. et al. [32,33] In summary, $CO_2$ electrochemical reaction was carried out at ambient

conditions using a filter-press electrochemical cell (Micro Flow Cell, ElectroCell A/S) in

continuous operation. The cell, shown in Fig. 1.b[17], was divided into a catholyte and

anolyte compartments separated by a Nafion 117 membrane. The airbrushed $Cu_2O/ZnO$-

catalyzed paper was employed as the working electrodes (geometric area, A= 10 $cm^{-2}$),

together with a platinized titanium plate used as the counter electrode and a Ag/AgCl (sat.

KCl) reference electrode. A 0.5 M KHCO3 (Panreac, > 97% purity) aqueous solution is

pumped at a flow rate of $Q_e/A$ = 2 ml $min^{-1}$ $cm^{-2}$ in both, the cathode and anode

compartments. Besides, $CO_2$ gas (99.99%) was fed to the cathode side with a flow rate

ranging from $Q_g/A$ = 10 to 20 ml $min^{-1}$ $cm^{-2}$. In addition, the applied current density, $j$, was

varied from 5 to 10 mA $cm^{-2}$. To quantify the concentration of each product in the liquid

phase, the samples were analysed by duplicate in a headspace gas chromatograph

(GCMS-QP2010, Ultra Shimadzu) equipped with a flame ionization detector (FID). The

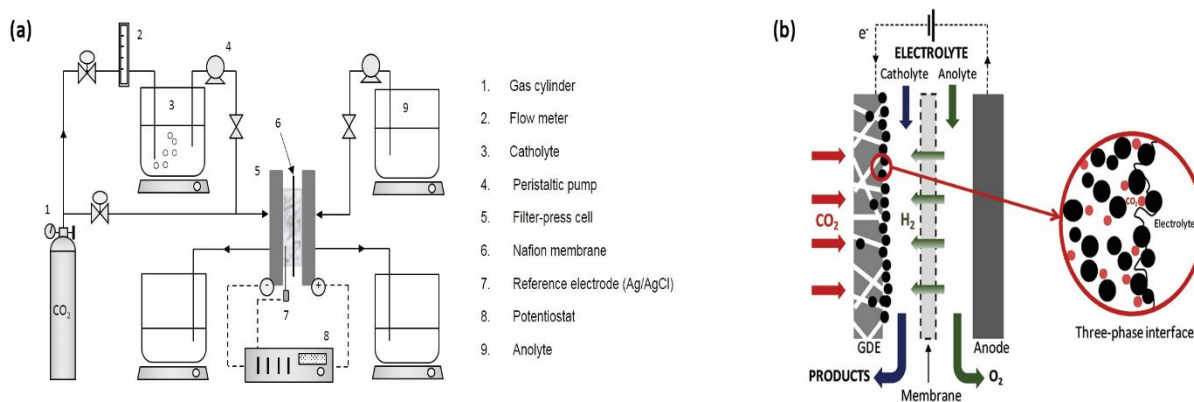formation rates and faradaic efficiencies are then calculated.

**Fig. 1.** (a) Experimental setup; (b) Schematic diagram of the electrolytic cell configuration

of $CO_2$ electrochemical reduction on $Cu_2O$-ZnO based GDE[17]

## 3.    Model Development

### 3.1.    Computational Domain

The domains of the present work are shown in Fig. 2. For simplification, the current

collectors and the cathode gas channel were excluded. The electrolyte stream enters the

cell via two channels (catholyte and anolyte). The catholyte flows through the porous

catalyst layer, at which the catholyte meets the gaseous $CO_2$ stream flowing from the

cathode gas channel through the GDL into the catalyst layer. Finally, the electrolyte,

products and unreacted materials leave the cell through the catholyte and anolyte outlets.

The key input parameters used in the model are listed in Table 2. The assumed properties

of catalyst layer in Table 2 are based on common values from the literature.[21,41,42]
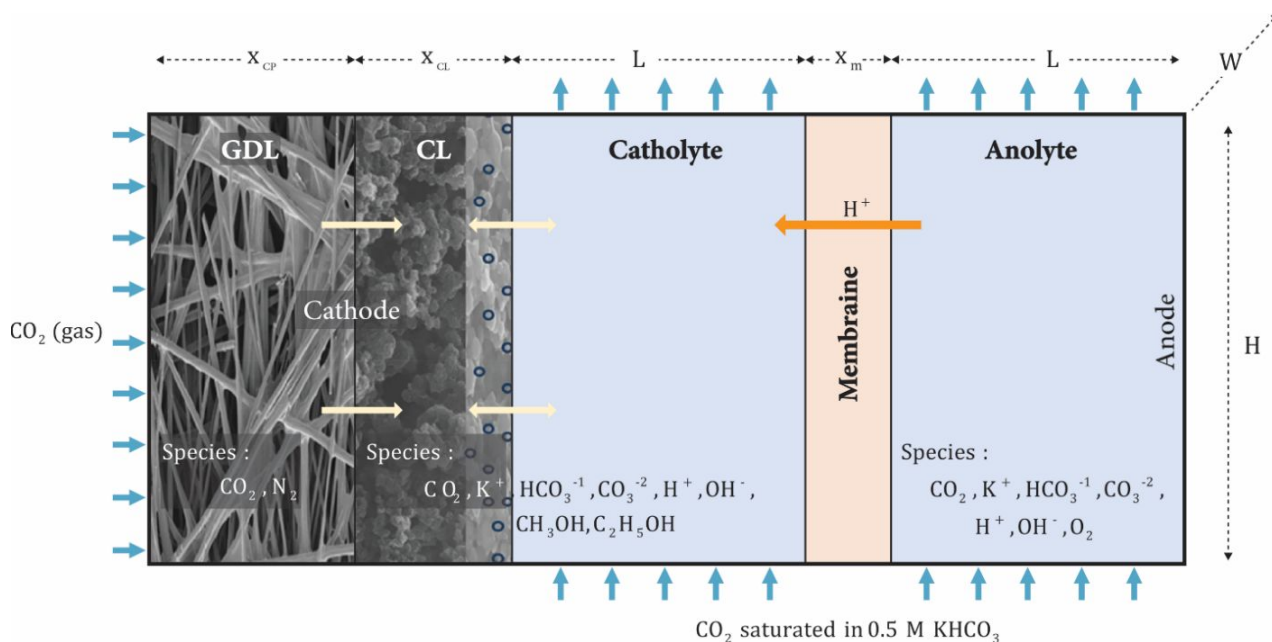


**Fig. 2.** Schematic diagram of the computational domain used in the present model.

### 3.2. Model Assumptions

The following were assumed in the present work:

– The system is steady-state.[24,38]

– The system is isothermal, i.e., the temperature distribution across the cell is

uniform.[24,38]

– Gas flow is considered to be compressible and laminar.

– Liquid flow is laminar.[38]

– Produced oxygen will completely dissolve in the electrolyte.

– The model is considered as a single-phase flow.

– The physical properties of the electrode are isotropic and homogeneous.[42]

– No-slip boundary condition is applied to all walls and continuity is maintained at electrolyte/porous media interface.

– Dilute theory is applied to the catholyte and anolyte.

– Proton transport from anode to cathode through the membrane is by electro-migration only.

– Convection through the catalyst layer is neglected and species are transported by diffusion and migration only.

– The carbon paper serving as the gas diffusion layer is considered hydrophobic.[43]

– Saturation through the catalyst layer is constant.

**Table 2**. Model parameters (see nomenclature for symbol definitions)

| Parameter | Value | Unit | Ref. |
|---|---|---|---|
| **Cell Dimensions** | | | |
| $A$ | 10 | cm$^2$ | 33 |
| $H$ | 33.3 | mm | 33 |
| $w$ | 30 | mm | 33 |
| $L$ | 4 | mm | 38 |
| $x_m$ | 0.183 | mm | 33 |
| $x_{cp}$ | 0.19 | mm | 44 |
| $x_{CL}$ | 0.02 | mm | Approximated |
| **Operating Conditions** | | | |
| $T$ | 25 | $^0$C | 33 |
| $P$ | 1 | Bar | 33 |
| $j_{app}$ | 10 | mA cm$^{-2}$ | 33 |
| $\varphi_c$ | -1.16 | V | 33 |
| $\varphi_a$ | 1.03 | V | 33 |
| $Q_e/A$ | 2 | ml min$^{-1}$ cm$^{-2}$ | 33 |
| $Q_g/A$ | 20 | ml min$^{-1}$ cm$^{-2}$ | 33 |
| **Membrane Properties** | | | |
| $\sigma_{l,m}$ | 10 | S m$^{-1}$ | 45 |
| $c_{H^+,m}$ | 1200 | mol m$^{-3}$ | 45 |

| Parameter | Value | Unit | Ref. |
|---|---|---|---|
| **Carbon Paper Properties** | | | |
| $\varepsilon_{cp}$ | 0.631 | 0.631 | [44] |
| $K_{cp}$ | $6.15 \times 10^{-12}$ | $m^2$ | [44] |
| $\sigma_{cp}$ | $1.053 \times 10^4$ | $S\,m^{-1}$ | [44] |
| **Catalyst Layer Properties** | | | |
| $K_{CL}$ | $1.58 \times 10^{-14}$ | $m^2$ | Assumption |
| $\varepsilon_{cL}$ | 0.4 | | Assumption |
| $x_{CL}$ | 0.02 | mm | Assumption |
| $r_p$ | 4 | $\mu m$ | [33] |
| $\sigma_{cL}$ | $10^{-5}$ | $S\,m^{-1}$ | Assumption |
| $\delta_{Tf}$ | 10 | nm | [21] |
| $s_{CL}$ | 0.5 | | Assumption |
| **Gas Properties** | | | |
| $M_{CO_2}$ | 44.009 | $Kg\,mol^{-1}$ | |
| $M_{N_2}$ | 28.0134 | $Kg\,mol^{-1}$ | |
| $\rho_{CO_2}$ | 1.98 | $kg\,m^{-3}$ | |
| $\mu_{CO_2}$ | $1.5 \times 10^{-5}$ | Pa s | |
| $H_{CO_2}$ | $3.3 \times 10^{-4}$ | $mol\,m^{-3}\,Pa^{-1}$ | |

| Parameter | Value | Unit | Ref. |
|---|---|---|---|
| $\nu_{CO_2}$ | 26.9 | | 46 |
| $\nu_{N_2}$ | 17.9 | | 46 |
| $Y_{CO_2,in}$ | 0.9999 | | 33 |
| **Liquid Electrolyte Properties** | | | |
| $\rho_{H_2O}$ | $10^3$ | kg m$^{-3}$ | |
| $\mu_{H_2O}$ | 8.9 x $10^{-4}$ | Pa s | |
| **Equilibrium Constants** | | | |
| $K_2$ | 4.66 | m$^3$/mol | 38 |
| $K_3$ | 4.44 x $10^{-4}$ | mol/m$^3$ | 38 |
| $K_w$ | $10^8$ | m$^6$/mol$^2$ | 38 |

### 3.3.   Bulk solution equilibrium

When gaseous $CO_2$ comes in contact with aqueous solution, $CO_2$ starts to dissolve in the solution as hydrated $CO_{2\,(aq)}$ according to eq (1). $CO_2$ in its dissolved form can react with water in a later step as in eqs (2) and (3).[47]

$$CO_{2_{(g)}} \leftrightarrow CO_{2(aq)} \tag{1}$$

Throughout the aqueous solution, the homogeneous acid-base reactions are assumed to be in equilibrium[38], eqs (2)-(4).

$$HCO_3^- + OH^- \leftrightarrow CO_3^{2-} + H_2O \qquad K_2 \qquad (2)$$

$$CO_{2_{aq}} + H_2O \leftrightarrow HCO_3^- + H^+ \qquad K_3 \qquad (3)$$

$$H^+ + OH^- \leftrightarrow H_2O \qquad K_w \qquad (4)$$

where $K_2$, $K_3$, and $K_w$ are the equilibrium constants, listed in Table 2.

### 3.4. Electrochemical Reactions

High purity $CO_2$ (99.99%) with 0.01 % $N_2$ is fed into the cathode gas channel. $CO_2$ will then diffuse through the gas diffusion layer into the cathode catalyst layer where the reduction reactions occur. In this electrochemical cell, potassium bicarbonate is used as an electrolyte. If sufficiently negative cell potential is applied, the $CO_2$ will react with the $H^+$ ions, produced by water oxidation at the anode, eq (5), and it will be reduced to $CH_3OH$ and $C_2H_5OH$, eqs (6) and (7). Hydrogen evolution reaction (HER), eq (8), may occur and is considered a competing reaction, as it consumes the $H^+$ ions necessary for $CO_2$ conversion to $CH_3OH$ and $C_2H_5OH$.

Anodic Reaction:

$$10\ H_2O \leftrightarrow 5\ O_2 + 20\ H^+ + 20\ e^- \tag{5}$$

Cathodic Reactions:

$$CO_2 + 6\ H^+ + 6\ e^- \leftrightarrow CH_3OH + H_2O \tag{6}$$

$$2\ CO_2 + 12\ H^+ + 12\ e^- \leftrightarrow C_2H_5OH + 3\ H_2O \tag{7}$$

$$2\ H^+ + 2\ e^- \leftrightarrow H_2 \tag{8}$$

## 3.5.  Governing Equations

The governing equations of the various regions in the electrochemical cell are summarized below.

### 3.5.1. Electrolyte Channels

#### 3.5.1.1.     Fluid Flow

The steady, 2D Newtonian laminar flow in the electrolyte channels (catholyte & anolyte) is governed by the continuity and Navier-Stokes equations[24], eqs (9) and (10)

$$\nabla . (\rho \boldsymbol{u}) = 0 \tag{9}$$

$$\rho \boldsymbol{u} \cdot \nabla \boldsymbol{u} = \rho g - \nabla p + \cdot \left[ \mu(\nabla \boldsymbol{u} + (\nabla \boldsymbol{u}))^T - \frac{2}{3}\mu(\nabla . \boldsymbol{u})\boldsymbol{I} \right] + \boldsymbol{F_v} \tag{10}$$

where $\rho$ is the density, $\boldsymbol{u}$ is the velocity vector, g is the gravitational acceleration, $p$ is the pressure, $\mu$ is the dynamic viscosity, $\boldsymbol{I}$ is the identity tensor, and $\boldsymbol{F_v}$ is the volume force vector.

### 3.5.1.2.    Mass Transport

Basically, the mass transport for an individual aqueous species $i$ through the electrolyte is governed by equation (11).

$$\nabla.\boldsymbol{N_i} = R_i \tag{11}$$

$$i = CO_2 , K^{+1}, HCO_3{}^{-1}, CO_3{}^{-2}, H^{+1}, OH^{-1}, CH_3OH , C_2H_5OH, O_2$$

$\boldsymbol{N_i}$ represents the flux vector of species $i$, and is governed by the Nernst-Plank equation[48], eq (12).

$$\boldsymbol{N_i} = -D_i\nabla c_i - z_i u_{m,i} F c_i \nabla \varphi_l + \boldsymbol{u} c_i \tag{12}$$

where $R_i$ is the production or consumption rate expression for species $i$, $c_i$ is the concentration of species $i$ , $F$ is the Faraday constant, $\varphi_l$ is the electric potential of the liquid electrolyte, and $D_i$ and $z_i$ are the diffusion coefficient and charge number of species $i$, respectively, listed in Table 3.

**Table 3.** Electrolyte liquid species and their properties

| Species | $D_i$ (cm$^2$ s$^{-1}$) | $z_i$ | Ref. |
|---|---|---|---|
| $CO_{2\,aq}$ | 1.92 x 10$^{-5}$ | 0 | 49 |
| $H^+$ | 9.311 x 10$^{-5}$ | +1 | 48,50 |
| $OH^{-1}$ | 5.273 x 10$^{-5}$ | -1 | 48,50 |
| $K^{+1}$ | 1.957 x 10$^{-5}$ | +1 | 48,50 |
| $HCO_3^{-1}$ | 1.185 x 10$^{-5}$ | -1 | 48,50 |
| $CO_3^{-2}$ | 0.923 x 10$^{-5}$ | -2 | 50 |
| $CH_3OH$ | 0.84 x1 0$^{-5}$ | 0 | 49 |
| $C_2H_5OH$ | 0.84 x 10$^{-5}$ | 0 | 49 |
| $O_2$ | 2.1 x 10$^{-5}$ | 0 | 49 |

The Nernst-Einstein relation[48], eq (13), is used for relating the ionic mobility, $u_{m,i}$, of the

ionic species to their diffusivity.

$$u_{m,i} = \frac{D_i}{RT} \tag{13}$$

where, $R$ is the gas constant, and $T$ is the absolute temperature.

Moreover, the current density vector $\boldsymbol{j}$ is proportional to the sum of all species fluxes as

expressed by Faraday's law[48], eq (14).

$$\boldsymbol{j} = F\sum_i z_i \boldsymbol{N}_i \tag{14}$$

### 3.5.1.3. Charge Transport

The Transport of protons from the anode to the cathode side is assumed to occur by electro-migration only. Furthermore, the charge conservation holds and electron transport can be described by Ohm's law, eqs (15) and (16).[48]

$$\nabla \cdot i_l = 0 \tag{15}$$

$$i_l = - \sigma_l \nabla \varphi_l \tag{16}$$

where $\sigma_l$ is the average ionic conductivity of the electrolyte, calculated from eq (17).[48]

$$\sigma_l = \left( \frac{F^2}{RT} \right) \left( \sum_i z_i^2 D_i c_i \right) \tag{17}$$

### 3.5.2. Cathode Gas Diffusion Layer (GDL)

### 3.5.2.1. Fluid Flow

The continuity equation, eq (18), and Brinkman momentum equation[24] (Brinkman's extension of Darcy's law), eq (19), were used for describing the pressure drop and gas flow within the porous GDL.

$$\rho \nabla \cdot (\boldsymbol{u}) = 0 \tag{18}$$

$$\frac{\rho}{\varepsilon} \boldsymbol{u} \cdot \nabla \frac{\boldsymbol{u}}{\varepsilon} = - \nabla p + \nabla \cdot \left[ \frac{\mu}{\varepsilon} (\nabla \boldsymbol{u} + (\nabla \boldsymbol{u})^T) - \frac{2}{3} (\nabla \cdot \boldsymbol{u}) \boldsymbol{I} \right] - \left( \frac{\mu}{k} \right) \boldsymbol{u} \tag{19}$$

where, $\rho$ is the gas mixture density, and $\varepsilon$ and $k$ are the porosity and permeability of the

porous media, respectively.

### 3.5.2.2.    Mass Transport

The multi-component mass transport in the porous GDL was solved to determine the

gas partial pressures at the gas-liquid interface. Maxwell-Stefan equation[51], eq (20) was

used for solving the fluxes of each species in terms of mass fraction.

$$R_i = \nabla.\left\{ -\rho\omega_i \sum_{i=1}^{n} D_{ij}^{eff} \left[ \frac{M_g}{M_j}\left( \nabla\omega_j + \omega_j\frac{\nabla M_g}{M_g} \right) + (x_j - \omega_j)\frac{\nabla P}{P} \right] + \rho u\omega_i \right\} \tag{20}$$

where, $\omega_i$ and $x_j$ are the mass and mole fraction, respectively, $M_g$ is the molar mass of

the gas mixture, eq (21), and $\rho$ is the ideal gas mixture density, described by eq (22).

$$M_g = x_{N_2}M_{N_2} + x_{CO_2}M_{CO_2} \tag{21}$$

$$\rho = (\sum_{i=1}^{N} X_i M_i P/(R.T) \tag{22}$$

where, $M_i$ is the molecular weight of species $i$.

The effective diffusivity, $D_{ij}{}^{eff}$, in eq (20) is corrected for the porosity, $\varepsilon$, and tortuosity,

$\tau$, of the considered porous medium using the Bruggeman relation, eq (23)

$$D_{ij}{}^{eff} = \frac{\varepsilon}{\tau} D_i = \varepsilon^{3/2} D_{ij} \tag{23}$$

where $D_{ij}$ can be estimated from the empirical correlation recommended by Fuller,

Schettler, and Giddings.[46]

$$D_{ij} = \frac{1.01325 \; x \; 10^{-2} T^{1.75} \left( \frac{1}{M_i} + \frac{1}{M_j} \right)^{0.5}}{P \left( v_i^{1/3} + v_j^{1/3} \right)^2} \tag{24}$$

where $v$ is the diffusion volume, listed in Table 2.

The mass fraction of $N_2$ is then calculated from the overall mass balance, eq (25).

$$\omega_{N_2} = 1 - \omega_{CO_2} \tag{25}$$

### 3.5.2.3.    Charge Transport

For the hydrophobic GDL (i.e. there is no electrolyte nor proton transport within the

GDL), charge is conserved. The electron transport through the solid phase was described

by Ohm's Law, eq (26).

$$\nabla \cdot i_s = 0 \tag{26}$$

where

$$i_s = -\sigma_{s,GDL} \nabla \varphi_s \tag{27}$$

where, $i_s$ is the current density of the solid phase of the GDL, $\sigma_{s,GDL}$ and $\varphi_s$ are the

electronic conductivity and the electric potential of the solid phase of the GDL,

respectively.

### 3.5.3. Cathode Catalyst Layer (CL)

As proposed by Lien-Chun Weng et al.[21], the triple-phase interface is not essential for

the high performance of the GDEs. In the present model, it was assumed that $CO_2$ first

dissolves into the aqueous solution within the CL, then reacts in its dissolved state. Based

on this assumption, the saturation volume fraction of the catalyst layer (i.e., the fraction

of liquid electrolyte covering the total pore volume of the porous catalyst layer) needs to

be accounted for. Therefore, the CL active area, $a_v$, available for the electroreduction

reactions was related to the saturation fraction $S_{CL}$, eq (28).[21]

$$a_v = a_v^0 S_{CL} \tag{28}$$

The catalyst layer was considered to contain spherical particles with radius $r_p$, with an intrinsic porosity $\varepsilon_{CL}^0$. The  specific surface area $a_v^0$  of the CL can be calculated from eq (29).[21]

$$a_v^0 = \frac{3(1 - \varepsilon_{CL}^0)}{r_p} \tag{29}$$

Due to the difficulty in saturation calculation, given the insufficient characteristics data available on the catalyst layer, a constant value of saturation fraction, $S_{CL}$ , was taken as shown in Table 2.

The porosity in eq (18) is modified according to eq (30).[21]

$$\varepsilon_{CL} = \varepsilon_{CL}^0(1 - S_{CL}) \tag{30}$$

### 3.5.3.1.          Mass Transport

Because of the extremely low velocity inside the porous media of the CL, the convection flux term in Nernst-Plank equation, eq (12), can be neglected. Therefore, the movement of the aqueous species is governed by diffusion and migration only, eq (31).

$$\boldsymbol{N_i} = -\, D_i^{eff}\nabla c_i - z_i u_{m,i} F c_i \nabla \varphi_l \tag{31}$$

The term $D_i^{eff}$ represents the effective diffusion coefficient of the aqueous species $i$, calculated using the Bruggeman relation, eq (23).

### 3.5.3.2. Charge Transport

For the CL, current can be split into two types; ionic current through the electrolyte, and electronic current through the catalyst particles. Similarly, the charge conservation equations can be calculated using Ohm's Law[21], eqs (32)-(34).

$$\nabla . i_s = - \nabla . i_l = - a_v \sum_k i_{loc,k} \tag{32}$$

$$i_l = - \sigma_l^{eff} \nabla \varphi_l \tag{33}$$

$$i_s = - \sigma_s^{eff} \nabla \varphi_s \tag{34}$$

where $i_{loc,k}$ is the local current density of electrode reaction with index $k$, $\sigma_s^{eff}$, $\sigma_l^{eff}$ are the effective conductivities of the solid and liquid phase, respectively, corrected by the Bruggeman correlation[21], eqs (35) and (36).

$$\sigma_l^{eff} = \varepsilon_l^{1.5} \sigma_l \tag{35}$$

$$\sigma_s^{eff} = \varepsilon_s^{1.5} \sigma_s \tag{36}$$

### 3.5.4. Membrane

As the work of Yosra et. al.[38], the membrane was modeled as a homogeneous medium containing fixed ionic charge with a molar concentration $c_{H^+,m}$. Charge conservation and Ohm's law are also applicable in the membrane domain;

$$\nabla . i_{l,m} = 0 \tag{37}$$

$$i_{l,m} = - \sigma_{l,m} \nabla \varphi_{l,m} \tag{38}$$

where, $\varphi_{l,m}$ is the membrane potential, and $\sigma_{l,m}$ is the membrane electric conductivity,

listed in Table 2.

At the membrane-electrolyte interfaces, the potential continuity was maintained through

considering the Donnan potential shift, $\nabla\varphi_D$. [38,53] It arises across the membrane as a result

of the differences in $H^+$ activity in the membrane, $a_{H^+,m}$, and the electrolyte, $a_{H^+,e}$. These

activities can be replaced by their corresponding concentrations $c_{H^+,m}$ and $c_{H^+,e}$, due to

the low concentration of ions, eq (39).[53]

$$\nabla\varphi_D = \varphi_{l,m} - \varphi_{l,e} = \frac{RT}{F} ln\left(\frac{c_{H^+,m}}{c_{H^+,e}}\right) \tag{39}$$

### 3.5.5. Electrochemical Kinetics

The electrochemical kinetic reactions at both cathode and anode can be described by

the modified Butler-Volmer equation, eq (40), also known as concentration-dependent

Butler-Volmer equation.

$$i_{loc,k} = i_{0,k}\left[\frac{C_{R,S}}{C_{R,B}}exp\left(\frac{\alpha_a z F}{R T}\eta\right) - \frac{C_{O,S}}{C_{O,B}}exp\left(\frac{\alpha_c z F}{R T}\eta\right)\right] \tag{40}$$

Here, $i_{0,k}$ is the equilibrium exchange current density of reaction $k$, $c_{R,S}$ and $C_{R,B}$ are the

surface and bulk concentrations of the reduced species, respectively, and $C_{O,S}$ and $C_{O,B}$

are the surface and bulk concentrations of the oxidized species, respectively. $\alpha_a$ and $\alpha_c$

represent the anodic and cathodic charge transfer coefficients, respectively, listed in

Table 4. The term $z$ represents the number of electrons transferred in the rate limiting-

step, and $\eta$ represents the activation overpotential.

**Table 4. Electrode Kinetics Parameters**

| Parameter | Symbol | Value | Unit |
|---|---|---|---|
| Charge transfer coefficients | | | |
| Anode | $\alpha_a$ | 0.5 | - |
| Cathode | $\alpha_c$ | 0.5 | - |
| Reference Conc. | $c_{ref}$ | 1 | mol l$^{-1}$ |
| Exchange Current Densities at Anode | | | |
| OER | $i_{0,OER}$ | 9.4223 | A m$^{-2}$ |

Similar to the work of Yosra et. al.[38], equation (40) can be reduced to the following

equations:

Anode side

$$i_{loc,\,OER} = i_{0,OER}\, exp\left(\frac{(\alpha_a + \alpha_c)\,F\eta}{RT}\right) \tag{41}$$

Cathode side

$$i_{loc,\ CH_3OH} = -\ i_{0,CH_3OH}\left(\frac{c_{co_2}\,c_{H^+}}{c^2_{ref}}\right)exp\left(\frac{-\alpha_c F\eta}{RT}\right) \tag{42}$$

$$i_{loc,\ C_2H_5OH} = -\ i_{0,C_2H_5OH}\left(\frac{c_{co_2}\,c_{H^+}}{c^2_{ref}}\right)exp\left(\frac{-\alpha_c F\eta}{RT}\right) \tag{43}$$

$$i_{loc,\ HER} = i_{0,HER}\left(\frac{(\alpha_a+\alpha_c)F}{RF}\right)\eta \tag{44}$$

Overpotential

$$\eta_k = \phi_s - \phi_l - E_{eq,k} \tag{45}$$

where, $c_{ref}$ is the reference concentration, and $E_{eq,k}$ is the equilibrium potential (Nernst

potential) of reaction $k$.

The exchange current densities in the above equations are obtained by fitting these

forms of Butler-Volmer equation to the current densities from the experimental results.

The model has related the exchange current density of the liquid products to the process

conditions through developing an empirical relation, eq (46).

$$i_{0,k} = i^*_{0,k}\left(\frac{j_{app}}{j^*}\right)^a\left(\frac{Q_g/A}{Q_g^*}\right)^b\left(\frac{Q_e/A}{Q_e^*}\right)^c \tag{46}$$

where $i^*_{0,k}$, $a$, $b$, and $c$ are the kinetics fitting constants.

The values of j*, $Q_g$*, and $Q_e$* are based on the optimum values from the experimental

work conducted by Albo et al. [17] ; $j$*= 10 mA cm$^{-2}$, $Q_g$*= 20 ml min$^{-1}$ cm$^{-2}$, and $Q_e$*=2 ml

min$^{-1}$ cm$^{-2}$.

The equilibrium potential $E_{eq,k}$ in eq (45) can be described by Nernst equation, eq (47).[54]

$$E_{eq,k} = E^0 + \frac{RT}{nF} ln \left[ \frac{a_{products}}{a_{reactants}} \right] \tag{47}$$

where, $E^0$ is the standard potential for the considered half-cell reaction, as shown in Table

5. The term $a$ represents the activity that can be replaced by the concentration, eqs (48)

and (49).

**Table 5.** Standard potentials for the considered electrochemical reactions

| Half-cell reaction | | $E^0$ | |
|---|---|---|---|
| OER | eq (5) | 1.23 | |
| CH$_3$OH | eq (6) | 0.02 | [$E^0$ vs. Ag/AgCL = $E^0$ vs. RHE - 0.059 PH - 0.197] [55] |
| C$_2$H$_5$OH | eq (7) | 0.08 | |
| HER | eq (8) | 0 | |

$E^0$ values are reported under standard conditions [1 atm and 250C] vs. reversible hydrogen electrode (RHE) in aqueous media.[56]

$$E_{eq, CH_3OH} = E^0_{CH_3OH} + \frac{RT}{6F} ln \left[ \frac{C_{CH_3OH}}{C_{CO_2} C_{H^+}^6} \right] \qquad \text{vs. Ag/AgCL} \tag{48}$$

$$E_{eq,\ C_2H_5OH} = E^0_{C_2H_5OH} + \frac{RT}{12F}ln\left[\frac{C^2_{C_2H_5OH}}{C^2_{CO_2}C^{12}_{H^+}}\right] \quad \text{vs. Ag/AgCL} \tag{49}$$

Therefore, the reaction source term $R_i$ in eq (11), can be calculated from the following

relations:

Anodic Reaction Source term:

$$R_{O_2} = \frac{vi_{loc,\ OER}}{20\ F} \tag{50}$$

Cathodic Reaction Source terms:

$$R_{CH_3OH} = \frac{a_v\,i_{loc,\ CH_3OH}}{6F} \tag{51}$$

$$R_{C_2H_5OH} = \frac{a_v\,i_{0,C_2H_5OH}}{12\ F} \tag{52}$$

$$R_{H_2} = \frac{a_v\,i_{loc,\ HER}}{2\ F} \tag{53}$$

where $v$ is the stoichiometric coefficient of $O_2$ in eq (5).

### 3.5.6. Rate of CO2 absorption-Film theory:

When the gaseous $CO_2$ comes into contact with the liquid electrolyte, at the GDL-CL

interface, it is absorbed into the electrolyte through a thin film. The steady-state flux

across this thin film can be described in terms of the gas-to-liquid mass transfer coefficient

$K_{GL,\ CO_2}$, eqs (54) and (55).[49]

$$N_{CO_2,abs} = K_{GL,\,CO_2}(c^*_{CO_2} - c_{CO_2}) \tag{54}$$

$$K_{GL,\,CO_2} = \frac{D_{CO_2}}{\delta_{Tf}} \tag{55}$$

where $N_{CO_{2,abs}}$ is $CO_2$ absorption flux relative to the interface, $c^*_{CO_2}$ and $c_{CO_2}$ are the

interfacial and bulk concentrations in the electrolyte, and $\delta_{Tf}$ is the thin-film thickness,

shown in Table 2.

$c^*_{CO_2}$ represents the solubility limit of $CO_2$ in the electrolyte and is proportional to the

partial pressure of $CO_2$ as stated by Henry's Law, eq (56).

$$c^*_{CO_2} = H_{CO_2}.p_g.Y_{CO_2} \tag{56}$$

Therefore,

$$N_{CO_2,\,abs} = K_{GL,\,CO_2}(H_{CO_2}.p_g.Y_{CO_2} - \beta.c_{CO_2}) \tag{57}$$

where $\beta$ is also a fitting parameter, used to differentiate the concentration of $CO_2$ in the

depletion boundary layer[57], at CL-GDL interface, from that of bulk electrolyte

concentration.

### 3.6. Boundary Conditions

The internal boundary conditions are given based on the continuity and mass flux balance to satisfy the general mass and species conservation of the entire cell. The boundary conditions at each interface are presented in details in Table 6.

**Table 6.** Boundary Conditions

| Position | Condition | |
|---|---|---|
| CGC-GDL Interface | Constant inlet gas velocity | $\boldsymbol{u} = - U_g^0$ |
| | Constant inlet gas composition | $Y_{CO_2} = Y_{CO_2,in}$ |
| | External applied current density | $j = j_{app}$ |
| Electrolyte Inlets | Constant inlet electrolyte velocity | $\boldsymbol{u} = - U_l^0 \boldsymbol{n}$ |
| | Constant inlet species concentrations | $- \boldsymbol{n}.\boldsymbol{N_i} = \boldsymbol{n}.(\boldsymbol{u} c_{i,in})$ |
| | Charge insulation | $- \boldsymbol{n}.\boldsymbol{i_l} = 0 \quad , \quad - \boldsymbol{n}.\boldsymbol{i_s} = 0$ |
| Electrolyte Outlets | Constant pressure (atmospheric) | $P = P_{atm}$ |
| | Zero-diffusive flux of species | $- \boldsymbol{n}.D_i \nabla c_i = 0$ |
| | Charge insulation | $- \boldsymbol{n}.\boldsymbol{i_l} = 0 \quad , \quad - \boldsymbol{n}.\boldsymbol{i_s} = 0$ |
| GDL-CL Interface | Species flux continuity ($CO_2$ is absorbed into the electrolyte) | $- \boldsymbol{n}.\boldsymbol{N}_{CO_2} = N_{CO_2, abs.}$ |
| | Current conservation | $\boldsymbol{n}.\boldsymbol{i}_{s.GDL} = \boldsymbol{n}.\boldsymbol{i}_{s.CL}$ |

| Position | Condition | |
|---|---|---|
| | | $i_l = 0$ |
| CL-Catholyte Interface | Species flux continuity | $-\boldsymbol{n}.\boldsymbol{N_i} = \sum_m R_{i,m}$ , $R_i = \frac{v\, i_{loc}}{z_i F}$ , |
| | Ionic current conservation | $\boldsymbol{n}.\boldsymbol{i_{l.CL}} = \boldsymbol{n}.\boldsymbol{i_{l.e}}$ |
| Catholyte-Membrane Interface | Proton flux continuity | $\boldsymbol{n}.\boldsymbol{N_{H^+.e}} = \boldsymbol{n}.\frac{i_{l.m}}{F}$ |
| | Current conservation | $\boldsymbol{n}.\boldsymbol{i_{l.e}} = \boldsymbol{n}.\boldsymbol{i_{l.m}}$ |
| | Donnan potential | $\varphi_{l,m} = \varphi_{l,e} + \frac{RT}{F}\ln\left(\frac{c_{H^+.m}}{c_{H^+.e}}\right)$ |
| Anolyte-Membrane Interface | Proton flux continuity | $\boldsymbol{n}.\boldsymbol{N_{H^+.e}} = \boldsymbol{n}.\frac{i_{l.m}}{F}$ |
| | Current conservation | $\boldsymbol{n}.\boldsymbol{i_{l.e}} = \boldsymbol{n}.\boldsymbol{i_{l.m}}$ |
| | Donnan Potential | $\varphi_{l,m} = \varphi_{l,e} + \frac{RT}{F}\ln\left(\frac{c_{H^+.m}}{c_{H^+.e}}\right)$ |
| Anode Surface | Species flux continuity | $-\boldsymbol{n}.\boldsymbol{N_i} = \sum_m R_{i,m}$ , $\boldsymbol{R_i} = \frac{v\, i_{loc}}{z_i F}$ |
| | External applied potential | $\boldsymbol{\varphi_{s,ext}} = \boldsymbol{\varphi_a}$ |
| | Current conservation | $\boldsymbol{n} . \boldsymbol{i_l} = i_{total} = \sum_m i_{loc,m}$ |
| Walls | No-slip boundary condition | $\boldsymbol{u} = 0$ |
| | No Flux | $-\boldsymbol{n}.\boldsymbol{N_i} = 0$ |
| | Charge insulation | $-\boldsymbol{n}.\boldsymbol{i_l} = 0$ , $-\boldsymbol{n}.\boldsymbol{i_s} = 0$ |

The concentrations of the different species entering the electrolyte $c_{i,in}$ were previously calculated in the work of Yosra, et. al.[38] from the equilibrium constraints along with the carbon balance and electroneutrality condition.

### 3.7.  Cell Performance - Faradaic Efficiency (FE)

Faradaic efficiency (FE), the selectivity of a reaction towards a particular product, is a good indication of cell performance. While HER is the side reaction, the faradaic efficiency for other products can be calculated as follows:

$$FE_{CH_3OH}(\%) = \frac{i_{CH_3OH}}{i_{total}} x\ 100 \tag{58}$$

$$FE_{C_2H_5OH}(\%) = \frac{i_{C_2H_5OH}}{i_{total}} x\ 100 \tag{59}$$

where the average total current density, $i_{total}$, equals the sum of the average current densities for all of the cathodic reactions:

$$i_{total} = \sum_m i_{loc,m} = i_{CH_3OH} + i_{C_2H_5OH} + i_{HER} \tag{60}$$

### 3.8.  Numerical method

The previous governing equations together with the boundary and inlet conditions were solved simultaneously using a commercially available software package, COMSOL

Multiphysics® v5.2. A user-defined mesh with mapped distribution was used in each

domain (i.e., the GDL, CL, catholyte, membrane, and anolyte domains). The number of

elements for each domain was varied according to the accuracy required in the solution.

The final mesh, contained 375 quad elements, 140 edge elements and 12 vertex

elements with a minimum and average element equal to unity. The model was solved

with the base case parameters, using the built-in  direct solver PARDISO (Parallel Sparse

Direct Solver), with a relative tolerance of 0.001, and a total of 9324 of degrees of freedom

through a fully coupled approach.

For this non-linear system to be converged, the stationary solver was divided into five

sequenced steps. In the "Free and Porous Media Flow" interface was solved first since

the solution of its equations is not affected by other interfaces in the model. Then, its

solution is stored to describe the velocity field for the Maxwell-Stefan and Nernst-Plank

equations. Secondly, the "Transport of Concentrated Species" interface together with the

flow coupling was solved. Afterwards, the two "Secondary Current Distribution" interfaces

were solved for both the electrolyte and membrane to estimate their electric fields.

Consequently, their solution was stored to describe the migration-diffusion equation. The

pre-mentioned solution was used as an initial value for the dependent variables in the

"Transport of Diluted Species" interface to get the concentration distribution. Finally, all

the interfaces were solved simultaneously to get the final results. Finally, parametric

sweeps were used for investigating the effect of changing cell operating conditions on its

performance.

## 4.    Results & Discussion

### 4.5.    Experimental Results

The use of $Cu_2O$-based GDEs for the electrochemical reduction of $CO_2$ led primarily to

the formation of $CH_3OH$, together with small quantities of $C_2H_5OH$. The results presented

by Albo et. al., 2016 [33] were used for validation. Besides, additional experimental tests

were carried out to validate the model. $CH_3OH$ production rate and Faradaic efficiency

(FE) were calculated at different applied current densities and gas flow rates, and results

are presented in Tables 7 and 8.

**Table 7.** Rate and FE of $CH_3OH$ and $C_2H_5OH$ using $Cu_2O$-ZnO GDEs as a function of j,

at $Q_e/A$ = 2 ml min$^{-1}$ cm$^{-2}$, and $Q_g/A$ = 20 ml min$^{-1}$ cm$^{-2}$

| E | j | Rate ($\mu$mol m$^{-2}$ s$^{-1}$) | | FE (%) | |
|---|---|---|---|---|---|
| (V) | (mA cm$^{-2}$) | CH$_3$OH | C$_2$H$_5$OH | CH$_3$OH | C$_2$H$_5$OH |
| -0.89 | 6 | 21.0 | 2.15 | 24.3 | 4.9 |
| -1.02 | 8 | 37.6 | 2.64 | 43.5 | 6.1 |
| -1.19 | 9 | 48.4 | 3.58 | 56 | 8.3 |

**Table 8.** Rate and FE for $CO_2$ electrochemical reduction to $CH_3OH$ at different gas flow

rates ($Q_g/A$) with $Cu_2O$/ZnO GDEs, at j = 10 mA cm$^{-2}$, $Q_e/A$ = 2 ml min$^{-1}$ cm$^{-2}$

| E (V) | $Q_g/A$ (ml min$^{-1}$ cm$^{-2}$) | Rate ($\mu$mol m$^{-2}$ s$^{-1}$) | FE (%) |
|---|---|---|---|
| -1.77 | 12.5 | 28.5 | 16.5 |
| -1.58 | 15 | 41.3 | 23.9 |
| -1.38 | 17.5 | 51.1 | 29.6 |

4.6.    Parametric Estimation and Model Validation

Values from the literature[38] were used as a starting point for the first round of calculation of the kinetics fitting parameters, then a trial and error method was applied together with COMSOL parametric sweeps. Percentage error[24] was calculated according to eq (61),

$$error_i. (\%) = \frac{r_i^{num.} - r_i^{exp.}}{r_i^{exp.}} \, x \, 100\% \tag{61}$$

Here, the subscript $i$ presents a single point at which the production rate was calculated.

The kinetic fitting constants in eq (46) were obtained by minimizing the percentage error between the resulting production rate of model and experiment while varying the applied current density. The fitting constants are listed in Table 9.

**Table 9.** Fitting parameters in the electrochemical reduction kinetic equations

| Parameter | Symbol | Value | Unit |
|---|---|---|---|
| **Exchange Current Densities at Cathode** | | | |
| Methanol | $i_{0,CH_3OH}^*$ | $1.335 \times 10^{10}$ | A.m$^{-2}$ |
| Ethanol | $i_{0,C_2H_5OH}^*$ | $3.070 \times 10^{10}$ | A.m$^{-2}$ |
| | $a$ | 2 | - |
| | $b$ | 1 | - |
| | $c$ | 0.5 | - |
| HER | $i_{0,HER}$ | $10^3$ | A.m$^{-2}$ |

| Parameter | Symbol | Value | Unit |
|-----------|--------|-------|------|
| Conc. fraction | $\beta$ | 0.004 | - |

## 4.7. Effect of Applied Current Density

Model validation was performed by comparing the effect of varying the applied current density, j, from 5 to 10 mA cm$^{-2}$, on the production rate and the faradaic efficiency, FE, of CH$_3$OH and C$_2$H$_5$OH, as shown in Fig. 3. Flow rates of both the electrolyte and the CO$_2$ were kept constant at Q$_e$/A = 2 ml min$^{-1}$ cm$^{-2}$ and Q$_g$/A = 20 ml min$^{-1}$ cm$^{-2}$, respectively.

According to Fig. 3.a, the production rate of CH$_3$OH and C$_2$H$_5$OH depends on the amount of applied current density; as the current density increases, the production rate of both CH$_3$OH and C$_2$H$_5$OH increases up to a current density of 9 mA cm$^{-2}$. After this value, a shift between the measured experimental and modeling results was observed. The same trend was obtained when comparing modeling results of faradaic efficiency, FE, with experimental ones, as shown in Fig. 3.b. An interesting fit between modeling and experimental results was maintained, after which a shift in the results was observed after an applied current density of nearly 9 mA cm$^{-2}$.
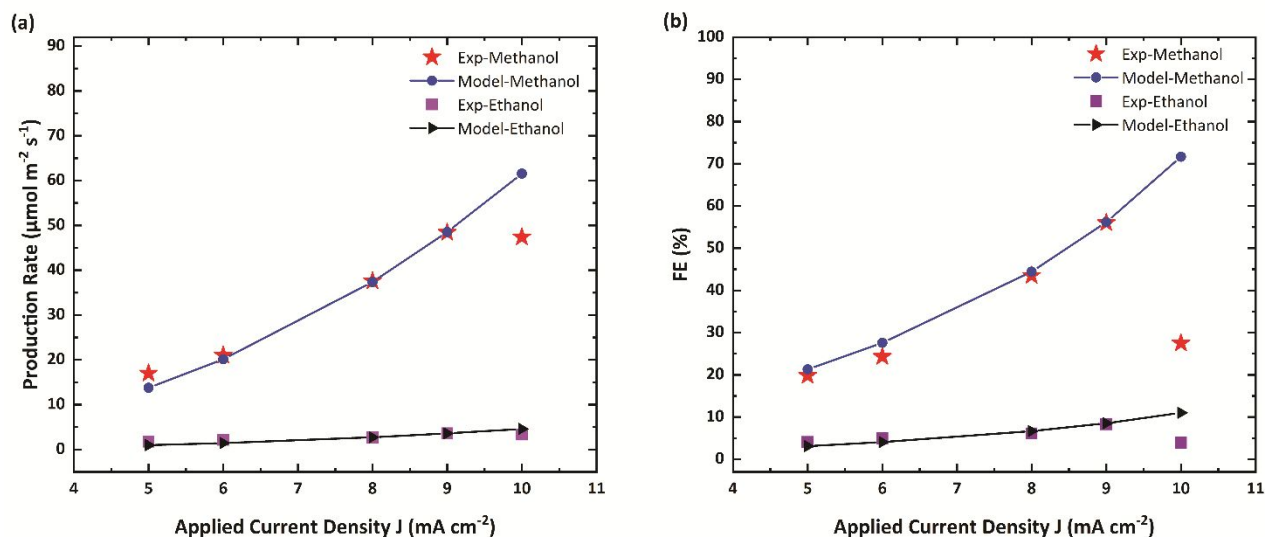
**Fig. 3.** Effect of applied current density on (a) Production rate of $CH_3OH$ and $C_2H_5OH$,

and (b) FE of $CH_3OH$ and $C_2H_5OH$, at constant $Q_e/A$ = 2 ml min$^{-1}$ cm$^{-2}$, and $Q_g/A$ = 20 ml

min$^{-1}$ cm$^{-2}$

This may be attributed to the accumulation of the products near the electrode which

limits the available $CO_2$ for further reaction, as outlined by Weng et al.[21] and Albo et al.[17,37]

Hence, a drop in the production rate and faradaic efficiency, FE, of both $CH_3OH$ and

$C_2H_5OH$ was observed, as shown in Fig. 3. When using GDE, mass transfer limitation is

greatly reduced and will occur at a relatively high current density compared to that of a

planner electrode, according to Weng et al.[21] and Castillo et al.[58] Experimental results in

Fig. 3, show that a limiting current density, $i_l$, was approached at nearly 9 mA cm$^{-2}$ that

caps the $CH_3OH$ production rate to nearly 50 µmol $m^{-2}$ $s^{-1}$. In the present model, the

limiting current density was not accounted for, as the Nernst diffusion layer thickness is

unknown, hence, the difference between the experimental and the modeling data

occurred after the 9 mA $cm^{-2}$ current density. This may be considered for future

development of the current work.

Moreover, the increase in the applied current density reflects an increase in system

energy. However, this energy is consumed by side reactions[17,21,37], such as the HER due

to water hydrolysis, or CO production instead of $CH_3OH$ production, which was not

accounted for in the model. This may interpret the shift in selectivity data that was

measured experimentally after the 9 mA $cm^{-2}$ applied current density, Fig. 3.

According to the literature[17], Cu-based GDEs are more selective to $CH_3OH$ formation

over $C_2H_5OH$. This was confirmed experimentally and captured by the model, as shown

in Fig. 3. When using $Cu_2O$-ZnO GDE, nearly 56% FE of $CH_3OH$ was obtained compared

to 8% maximum FE for $C_2H_5OH$.

In general, results obtained from the model and the experimental setup are consistent.

The root mean squared error (RMSE) between the experimental and simulated average

production rates were calculated according to eq (62). The RMSE together with the

percentage error, eq (61)[24], gives an indication of the accuracy of the model.

$$RMSE = \sqrt{\frac{1}{N} \sum_{k=1}^{N} \left(r_{total}^{num} - r_{total}^{exp}\right)^2} \tag{62}$$

A root mean squared error (RMSE) of 1.69 µmol m$^{-2}$ s$^{-1}$ and an average percentage error

of 6 % were obtained. This reflects a good agreement between the model and the

experimental results.

## 4.8. Effect of Gas Flow Rate

The relation between the production rate and selectivity, FE, of $CH_3OH$ and gas flow

rate, $Q_g$, was investigated, as shown in Fig. 4. The applied current density and the

electrolyte flow rate were kept constant at j = 9 mA cm$^{-2}$, and $Q_e$/A = 2 ml min$^{-1}$ cm$^{-2}$,

respectively. It was found that the production rate and FE of $CH_3OH$ increase as the flow

rate of feed $CO_2$ increases. This was compared with the results obtained through

experimental testing and there was a good consistency until a gas flow rate value of 17.5

ml min$^{-1}$ cm$^{-2}$, after which the production rate and selectivity, FE, no longer increase with

the increase in the gas flow rate, opposite to the modeled trend at that point.
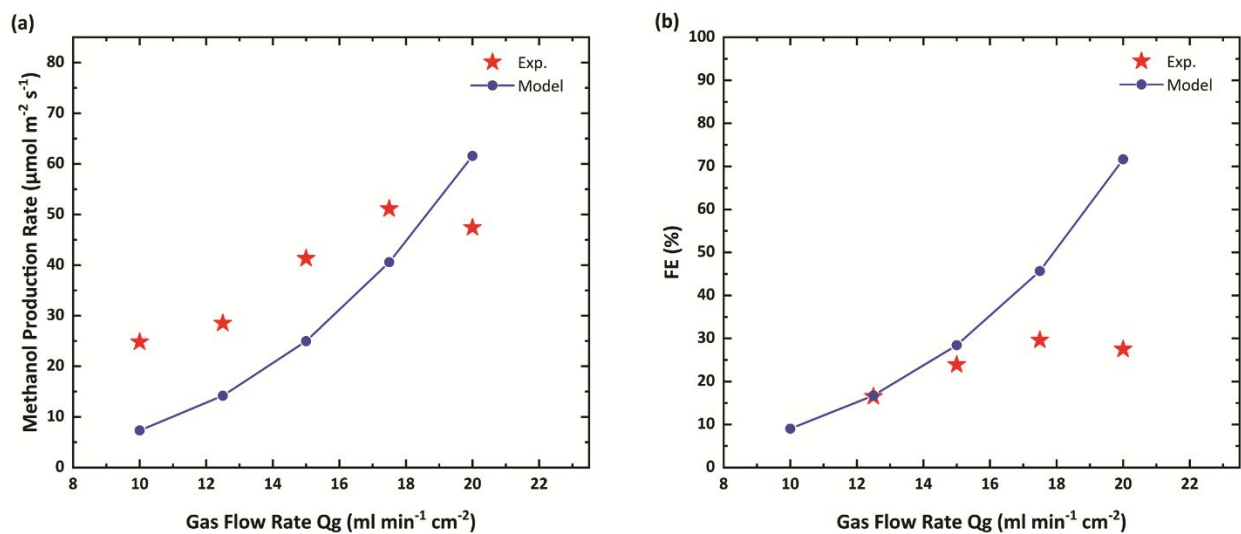
**Fig. 4.** Effect of Gas flow rate on (a) $CH_3OH$ production rate, and (b) FE of $CH_3OH$, at

constant j =10 mA cm$^{-2}$, and $Q_e$/A = 2 ml min$^{-1}$ cm$^{-2}$

Assuming constant CL saturation in the model could have caused such deviation

between the modeling and experimental results. As the gas flow rate increases, it is

believed that the CL saturation, $S_{CL}$ , percentage will decrease. Increasing the $CO_2$ flow

rate will cause the electrolyte layer to become thinner, which will reduce the mass transfer

barrier as outlined by Weng et al.[21] Hence the production rate of the $CH_3OH$ increases

with the increase in the $CO_2$ gas flow rate. However, further increase in the gas flow rate

to higher levels will interfere with the spreading of the electrolyte layer and the three-

phase interface through the CL may disappear (i.e., $S_{CL}$= zero) in some places, so, the

production rate will drop.[21]

In another case scenario, Albo et al.[17,37] attributed such reduction in the production rate

and FE of $CH_3OH$ to the deterioration caused by the detachment of the catalyst metal

particles after continuous operation at high flow rate. This will alter the catalyst stability

causing reduction at such high flow rate. High gas flow rates would cause excessive gas

penetration into the catholyte channel, disturbing the flow, and lowering the stability of the

cell.[59] This can be considered to identify the optimum working inlet gas flow rate during

the design of GDE based electrochemical cell.

### 4.9.   Effect of Electrolyte Flow Rate

The effect of increasing the electrolyte flow rate by several orders of magnitude on the

$CH_3OH$ production rate was investigated, as shown in Fig. 5. The model was able to

capture the trend confirmed through the experimental testing by developing an empirical

eq (46). At low electrolyte flow rates, the production rate of $CH_3OH$ was nearly constant,

as confirmed in the literature.[17,18,32,58] However, when the electrolyte flow rate increased,

the production rate increased rapidly in agreement with Weng et al.[18].
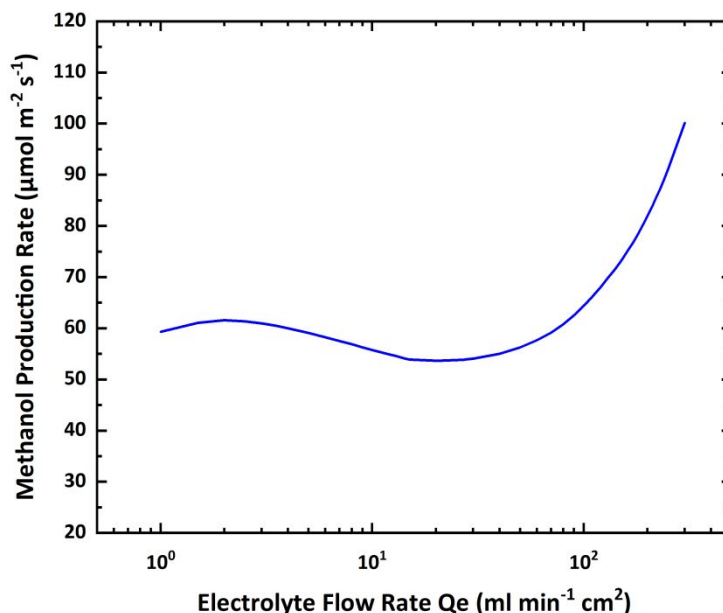


Fig. 5. Effect of electrolyte flow rate on $CH_3OH$ production rate, at constant j = 10 mA

$cm^{-2}$, and $Q_g/A$ = 20 ml $min^{-1}$ $cm^{-2}$

At low electrolyte flow rate, it is expected that the dominant force in the porous CL is

the capillary force, where $CO_2$ will be available in the middle of the CL pores separated

from the electrode surface by a layer of electrolyte. At this condition, the $CH_3OH$

production rate was relatively constant, as in Fig. 5. However, as the electrolyte flow rate

increase, it is expected that the capillary number will increase, elevating the possibility

that a shift in the dominant force toward viscous forces at very high electrolyte flow rate.

At this condition, the production of $CH_3OH$ starts to increase rapidly. Hence, economic

wise it is recommended to work at low electrolyte flow rate to obtain high concentrated

liquid products, lower the operating cost, and avoid excessive electrolyte wastes.[59]

Combining the findings of the present research regarding the effect of increasing the

$CO_2$ gas flow rate, Fig. 4, and electrolyte flow rate, Fig. 5, it is believed that in the GDE

based electrochemical cell, $CO_2$ needs to dissolve first in the aqueous phase for the

reduction reaction to occur in agreement with Weng et al.[18]. However, at low electrolyte

flow rate the presence of the $CO_2$ as a gas phase is essential to improve the production

rate.

### 4.10. Effect of Feed $CO_2$ Concentration

Variable $CO_2$ sources are available for the electrochemical reduction of $CO_2$ to produce

$CH_3OH$. Though these sources are not of high purity. In addition, the concentration of

$CO_2$ varies from one source to another. Hence, it is important to study the effect of

variation in the concentration of $CO_2$ in the feed stream on the amount of $CH_3OH$ that

could be produced by the electrochemical reduction of $CO_2$.

In practice, the purification cost of $CO_2$ stream increases with the increase in the degree

of purity required, this means that obtaining a 100% pure $CO_2$ stream is too expensive

which will add up to the cost of the overall process. On the other hand, a stream of $CO_2$

of purity 90% and lower can be obtained at a relatively reasonable price. The model was

used to investigate the effect of increasing the concentration of $CO_2$ on the production

rate and FE of $CH_3OH$ at various applied current density and various gas flow rate within

the optimum range. According to Fig. 6 and 7, as the $CO_2$ concentration increases the

production rate and FE of $CH_3OH$ increases, however, a plateau is reached at $CO_2$

concentration of nearly 90%. In addition, as the $CO_2$ concentration increases, the effect

of increasing the gas flow rate and the applied current density increases. Hence, working

at 90% or slightly lower $CO_2$ concentration at optimum values of applied current density

and gas flow rate is recommended from the economic point of view.
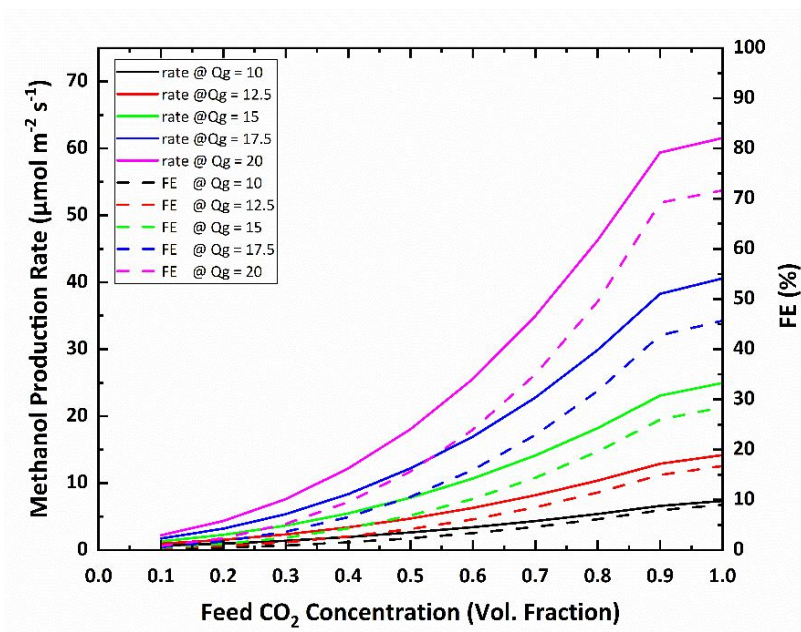
**Fig. 6.** Effect of feed $CO_2$ concentration on the production rate and FE of $CH_3OH$ as a function of gas flow rate ($Q_g$, ml min$^{-1}$ cm$^{-2}$), at constant j = 10 mA cm$^{-2}$, and $Q_e/A$ = 2 ml min$^{-1}$ cm$^{-2}$
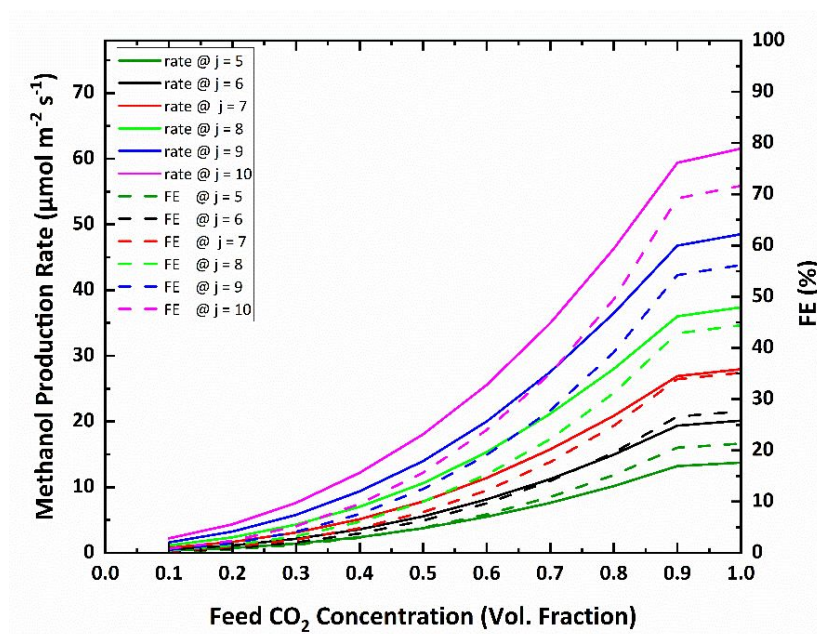
**Fig. 7.** Effect of feed $CO_2$ concentration on the production rate and FE of $CH_3OH$ as a function of applied current density (j, mA cm$^{-2}$) at constant $Q_g$=20 ml min$^{-1}$ cm$^{-2}$, and $Q_e/A$=2 ml min$^{-1}$ cm$^{-2}$

## 4.11. Product Distribution

Fig. 8 illustrates product distribution through the cell. $CH_3OH$, as well as $C_2H_5OH$, was found to be concentrated inside the CL and around the CL-catholyte interface, with zero concentration elsewhere. It is clear that $CH_3OH$ did not cross the membrane. $CH_3OH$ and $C_2H_5OH$ are produced at the cathode with different rates depending on the parameters in their kinetic rate equations, eqs (42) and (43).
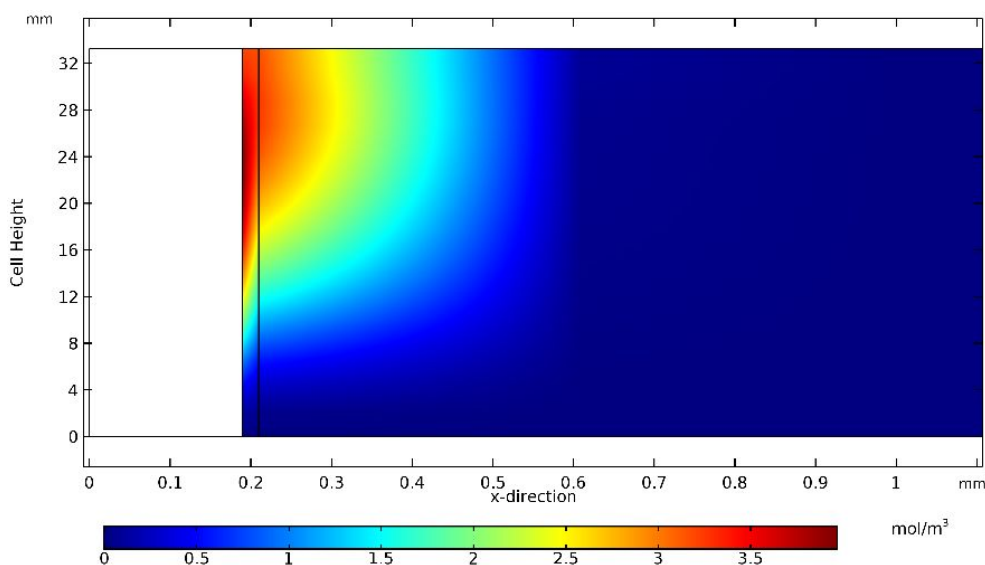
**Fig. 8.** Distribution of the concentration of $CH_3OH$, in mol $m^{-3}$, through the CL and

catholyte

In addition, Fig. 9 shows the production fluxes of the different species across the

cathodic CL. It is clear that the fluxes of $CH_3OH$ and $C_2H_5OH$ are function of the

concentration of the reactants at the surface of the cathode, so their production rate

reaches its maximum value at the center of the cell entrance. On the other hand, the rate

of $H_2$ production, shown in Fig. 9, is independent of the cathode position because it is not

affected by the availability of the reacting $CO_2$. In the electrochemical cell, the applied

current to the system was partially consumed by water reduction reaction rather than $CO_2$

reduction so, $H_2$ is produced continuously.
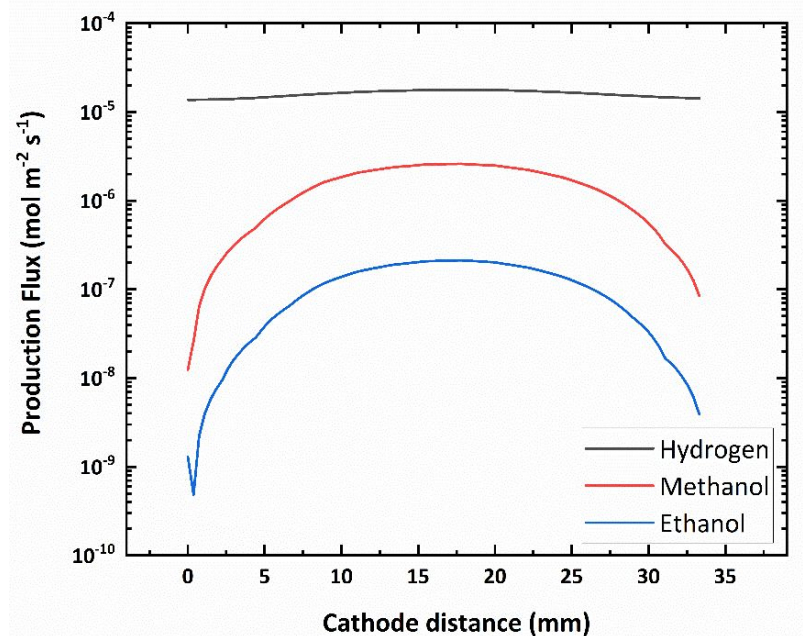
**Fig. 9.** The distribution of production flux of hydrogen, $CH_3OH$, and $C_2H_5OH$ across the

cathodic catalyst layer.

5.    Limitations of the Developed Model

   As far as we can tell, the present model is the first in investigating the role of GDEs in

the $CO_2$ electrochemical reduction into $CH_3OH$, where the exchange current density was

expressed as a function of the operating conditions. However, the model still has some

limitations restricting its ability to predict the effect of other process variables. These

limitations can be summarized as follows:

- The model cannot capture the variation of system selectivity with the change in system conditions.

- The distribution of reactants over the catalyst active sites cannot be determined accurately which introduces some uncertainty in the estimated parameters.

- The variation of saturation fraction in the CL with the change in the gas and electrolyte flow rate was neglected in the model. This limited the capabilities of the model to fully express the effect of flow rate variation on the system.

- Assuming one-phase flow hindered the model to predict the possibility of electrolyte penetration by the undissolved $CO_2$ gas or the production of $H_2$ in the gas phase.

Accordingly, these points could be considered as a recommendation for future development of a continuous $CO_2$ electrochemical reduction model for the production of $CH_3OH$ and other products.

## 6.    Conclusion

In this study, a mathematical model was developed for a continuous $CO_2$ electrochemical reduction cell for the production of $CH_3OH$, inside a filter-press electrochemical cell, equipped with $Cu_2O/ZnO$-based GDE, in 0.5 M $KHCO_3$ aqueous solution, under ambient conditions. It incorporated charge, mass and momentum transport with electrode kinetics, and considered the equilibrium reactions between the electrolyte species. Experiments were conducted using a relevant setup to validate the model. The model demonstrated the effect of key variables on production rate and faradaic efficiency. It was found that:

- The simulation results were in good agreement with the experimental results, with an average error of 6%.

- The production rate and the faradaic efficiency of both $CH_3OH$ and $C_2H_5OH$ increase with the increase in current density up to a value of 9 mA $cm^{-2}$. No further improvement in the $CH_3OH$ production rate above 50 µmol $m^{-2}$ $s^{-1}$ was obtained.

- $Cu_2O$-ZnO GDEs are more selective to $CH_3OH$ formation over $C_2H_5OH$; 56% faradaic efficiency of $CH_3OH$ was obtained compared to 8% maximum for $C_2H_5OH$.

- As the flow rate of feed $CO_2$ increases, the production rate and the faradaic efficiency of $CH_3OH$ increases up to an optimum value of 17.5 ml min$^{-1}$ cm$^{-2}$ after which the production rate and the selectivity will drop.

- Increasing the flow rate of the electrolyte did not affect $CH_3OH$ production at low flow rate. Only at very high electrolyte flow rate, the production of $CH_3OH$ started to increase rapidly.

- Working at low electrolyte flow rate is economic and more practical.

- At low electrolyte flow rate, the presence of the $CO_2$ as a gas phase is essential to improve the production rate.

- From the economic point of view, it is recommended to use a gas stream of 90% or slightly lower $CO_2$ concentration at optimum values of applied current density and gas flow rate.

As far as we can tell, this work is the first to model the GDE systems for $CO_2$ reduction into $CH_3OH$. In addition, it is the first 2D model that deals with the catalyst layer as a domain not as an interface, and the first to conclude an empirical relationship between the exchange current density and the operating conditions. In sum, the insights presented

in this model can be used as a guide for an effective design of GDE-based

electrochemical cells, and as a step for process scale-up and optimization.

## AUTHOR INFORMATION

### Corresponding Author

*Tel.: +201207370644. E-mail: omniaelshafie737@gmail.com

### ORCID

Omnia A. El-Shafie: 0000-0003-0735-6758

### Notes

The authors declare no competing financial interest.

## ACKNOWLEDGMENT

# List of symbols

## Roman

| | | |
|---|---|---|
| $A$ | Electrode geometric area, m$^2$ | |
| $a_i$ | Activity of species i, mol m$^{-3}$ | |
| $c_i$ | Concentration of species i, mol m$^{-3}$ | |
| $c_{ref}$ | Reference concentration, mol m$^{-3}$ | |
| $D_i$ | Diffusivity of species i, m$^2$ s$^{-1}$ | |
| $E^0$ | Reversible electrode potential, V | |
| $\boldsymbol{F_v}$ | Volume force vector, N m$^{-3}$ | |
| $F$ | Faraday's Constant, 96,487 C mol$^{-1}$ | |
| $FE$ | Faradaic Efficiency, % | |
| $g$ | Gravitational acceleration, m$^2$ s$^{-1}$ | |
| $H$ | Cell height, m | |
| $H_i$ | Henry constant of species i, mol m$^{-3}$ Pa$^{-1}$ | |
| $i_{loc}$ | Local current density, A m$^{-2}$ | |
| $i_{0,k}$ | Exchange current density of reaction k, A m$^{-2}$ | |
| $\boldsymbol{I}$ | Identity tensor | |
| $j$ | Current Density, A m$^{-2}$ | |
| $K$ | Permeability, m$^2$ | |
| $L$ | Thickness of each electrolyte channel, mm | |
| $M_i$ | Molecular weight of species i, kg mol$^{-1}$ | |

$N_i$ Flux vector of species $i$, mol m$^{-2}$ s$^{-1}$

$P$ Atmospheric pressure

$Q$ Flow rate, m$^3$ s$^{-1}$

$r$ radius, m

$R$ Gas constant, J mol$^{-1}$ K$^{-1}$

$R_i$ Rate of production or consumption for species $i$, mol m$^{-3}$ s$^{-1}$

$S$ Saturation

$T$ Temperature, K

$u$ Velocity vector, m s$^{-1}$

$u_{m,i}$ ionic mobility of species i, mol s kg$^{-1}$

$x_j$ thickness of domain j, m

$Y_j$ mole fraction of species i

$W$ Cell width, m

$z$ Number of electrons transferred

$z_i$ Charge number of species i

## Greek

$\alpha$ Charge transfer coefficient

$\delta$ thickness, m

$\eta$ Overpotential, V

$\mu$ Viscosity

$\rho$ Density, Kg m$^{-3}$

$\varepsilon$ Porosity

$\sigma$          Electric conductivity, S m$^{-1}$

$\varphi$          Potential, V

$\tau$          Tortuosity

$\nu$          Stoichiometric coefficient

$\nu_i$          Diffusion Volume of species i

$\omega_i$          Mass fraction of species $i$

## Subscript

$a$          Anode

$abs$          Absorbed

$aq$          Aqueous phase

$app$          Applied

$B$          Bulk

$c$          Cathode

$CO_2$          Carbon dioxide

$CO_3^{-2}$          Carbonate ion

$cp$          Carbon paper

$CL$          Catalyst layer

$D$          Donnan

$e$          Electrolyte

$eff$          Effective

$ext$          External

| | |
|---|---|
| $g$ | Gas |
| $GDE$ | Gas diffusion electrode |
| $GDL$ | Gas diffusion layer |
| $H^+$ | Hydrogen ion |
| $HCO_3^{-1}$ | Bicarbonate ion |
| $H_2O$ | Water |
| $i$ | Species |
| $in$ | Inlet |
| $K^+$ | Potassium ion |
| $l$ | Liquid phase |
| $m$ | Membrane |
| $O$ | Oxidized |
| $OH^+$ | Hydroxyl ion |
| $O_2$ | Oxygen |
| $p$ | particle |
| $R$ | Reduced |
| $ref$ | Reference value |
| $S$ | Surface or solid phase |
| $tf$ | Thin film |

## Superscript

| | |
|---|---|
| $exp.$ | Experimental |

*num.*   Numerical

*T*   Transpose

## REFERENCES

(1)   Song, C. Global Challenges and Strategies for Control, Conversion and Utilization of CO2 for Sustainable Development Involving Energy, Catalysis, Adsorption and Chemical Processing. *Catalysis Today* **2006**, *115* (1–4), 2–32. https://doi.org/10.1016/j.cattod.2006.02.029.

(2)   Friedlingstein, P.; Andrew, R. M.; Rogelj, J.; Peters, G. P.; Canadell, J. G.; Knutti, R.; Luderer, G.; Raupach, M. R.; Schaeffer, M.; van Vuuren, D. P.; et al. Persistent Growth of CO2 Emissions and Implications for Reaching Climate Targets. *Nature Geoscience* **2014**, *7* (10), 709–715. https://doi.org/10.1038/ngeo2248.

(3)   Qiao, J.; Liu, Y.; Zhan, J. *Electrochemical Reduction of Carbon Dioxide. Fundamentals and Technologies*; 2016.

(4)   Centi, G.; Perathoner, S. Opportunities and Prospects in the Chemical Recycling

of Carbon Dioxide to Fuels. *Catalysis Today* **2009**, *148* (3–4), 191–205. https://doi.org/10.1016/j.cattod.2009.07.075.

(5)     Centi, G.; Quadrelli, E. A.; Perathoner, S. Catalysis for CO2 Conversion: A Key Technology for Rapid Introduction of Renewable Energy in the Value Chain of Chemical Industries. *Energy and Environmental Science* **2013**, *6* (6), 1711–1731. https://doi.org/10.1039/c3ee00056g.

(6)     Albo, J.; Alvarez-Guerra, M.; Castaño, P.; Irabien, A. Towards the Electrochemical Conversion of Carbon Dioxide into Methanol. *Green Chemistry* **2015**, *17* (4), 2304–2324. https://doi.org/10.1039/C4GC02453B.

(7)     Rabiee, A.; Nematollahi, D. Pyridinium-Facilitated CO 2 Electroreduction on Pt Nanowire: Enhanced Electrochemical Performance in CO 2 Conversion. *Environmental Progress & Sustainable Energy* **2019**, *38* (1), 112–117. https://doi.org/10.1002/ep.12975.

(8)     Wang, R.; Kapteijn, F.; Gascon, J. Engineering Metal–Organic Frameworks for the Electrochemical Reduction of CO 2 : A Minireview. *Chemistry – An Asian Journal*

**2019**, *14* (20), 3452–3461. https://doi.org/10.1002/asia.201900710.

(9)     Malik, K.; Singh, S.; Basu, S.; Verma, A. Electrochemical Reduction of CO 2 for Synthesis of Green Fuel. *Wiley Interdisciplinary Reviews: Energy and Environment* **2017**, *6* (4), e244. https://doi.org/10.1002/wene.244.

(10)    Kaneco, S.; Hiei, N.; Xing, Y.; Katsumata, H.; Ohnishi, H.; Suzuki, T.; Ohta, K. Electrochemical Conversion of Carbon Dioxide to Methane in Aqueous NaHCO3 Solution at Less than 273 K. *Electrochimica Acta* **2002**, *48* (1), 51–55. https://doi.org/10.1016/S0013-4686(02)00550-9.

(11)    Morrison, A. R. T.; van Beusekom, V.; Ramdin, M.; van den Broeke, L. J. P.; Vlugt, T. J. H.; de Jong, W. Modeling the Electrochemical Conversion of Carbon Dioxide to Formic Acid or Formate at Elevated Pressures. *Journal of The Electrochemical Society* **2019**, *166* (4), E77–E86. https://doi.org/10.1149/2.0121904jes.

(12)    Hara, K.; Kudo, A.; Sakata, T.; Watanabe, M. High Efficiency Electrochemical Reduction of Carbon Dioxide under High Pressure on a Gas Diffusion Electrode Containing Pt Catalysts. *Journal of The Electrochemical Society* **1995**, *142* (4),

L57–L59. https://doi.org/10.1149/1.2044182.

(13) Piontek, S.; junge Puring, K.; Siegmund, D.; Smialkowski, M.; Sinev, I.; Tetzlaff, D.; Roldan Cuenya, B.; Apfel, U.-P. Bio-Inspired Design: Bulk Iron–Nickel Sulfide Allows for Efficient Solvent-Dependent $CO_2$ Reduction. *Chemical Science* **2019**, *10* (4), 1075–1081. https://doi.org/10.1039/C8SC03555E.

(14) Aeshala, L. M.; Rahman, S. U.; Verma, A. Effect of Solid Polymer Electrolyte on Electrochemical Reduction of $CO_2$. *Separation and Purification Technology* **2012**, *94*, 131–137. https://doi.org/10.1016/j.seppur.2011.12.030.

(15) Sebastián, D.; Palella, A.; Baglio, V.; Spadaro, L.; Siracusano, S.; Negro, P.; Niccoli, F.; Aricò, A. S. $CO_2$ Reduction to Alcohols in a Polymer Electrolyte Membrane Co-Electrolysis Cell Operating at Low Potentials. *Electrochimica Acta* **2017**, *241*, 28–40. https://doi.org/10.1016/j.electacta.2017.04.119.

(16) Bernardi, D. M. A Mathematical Model of the Solid-Polymer-Electrolyte Fuel Cell. *Journal of The Electrochemical Society* **1992**, *139* (9), 2477. https://doi.org/10.1149/1.2221251.

(17)  Albo, J.; Irabien, A. Cu2O-Loaded Gas Diffusion Electrodes for the Continuous

Electrochemical Reduction of CO2 to Methanol. *Journal of Catalysis* **2016**, *343*,

232–239. https://doi.org/10.1016/j.jcat.2015.11.014.

(18)  Weng, L. C.; Bell, A. T.; Weber, A. Z. Modeling Gas-Diffusion Electrodes for CO2

Reduction. *Physical Chemistry Chemical Physics* **2018**, *20* (25), 16973–16984.

https://doi.org/10.1039/c8cp01319e.

(19)  Kopljar, D.; Inan, A.; Vindayer, P.; Wagner, N.; Klemm, E. Electrochemical

Reduction of CO2 to Formate at High Current Density Using Gas Diffusion

Electrodes. *Journal of Applied Electrochemistry* **2014**, *44* (10), 1107–1116.

https://doi.org/10.1007/s10800-014-0731-x.

(20)  El-kharouf, A.; Mason, T. J.; Brett, D. J. L.; Pollet, B. G. Ex-Situ Characterisation of

Gas Diffusion Layers for Proton Exchange Membrane Fuel Cells. *Journal of Power

Sources* **2012**, *218*, 393–404.

https://doi.org/https://doi.org/10.1016/j.jpowsour.2012.06.099.

(21)  Weng, L.-C.; Bell, A. T.; Weber, A. Z. Modeling Gas-Diffusion Electrodes for CO 2

Reduction. *Physical Chemistry Chemical Physics* **2018**, *20* (25), 16973–16984.

https://doi.org/10.1039/C8CP01319E.

(22) Park, S.; Lee, J.-W.; Popov, B. N. A Review of Gas Diffusion Layer in PEM Fuel

Cells: Materials and Designs. *International Journal of Hydrogen Energy* **2012**, *37*

(7), 5850–5865. https://doi.org/10.1016/j.ijhydene.2011.12.148.

(23) Cook, R. L.; MacDuff, R. C.; Sammells, A. F. High Rate Gas Phase CO2 Reduction

to Ethylene and Methane Using Gas Diffusion Electrodes. *Journal of The*

*Electrochemical Society* **1990**, *137* (2), 607. https://doi.org/10.1149/1.2086515.

(24) Wu, K.; Birgersson, E.; Kim, B.; Kenis, P. J. A.; Karimi, I. A. Modeling and

Experimental Validation of Electrochemical Reduction of CO 2 to CO in a

Microfluidic Cell. *Journal of The Electrochemical Society* **2015**, *162* (1), F23–F32.

https://doi.org/10.1149/2.1021414jes.

(25) Yano, H.; Shirai, F.; Nakayama, M.; Ogura, K. Efficient Electrochemical Conversion

of CO2to CO, C2H4and CH4at a Three-Phase Interface on a Cu Net Electrode in

Acidic Solution. *Journal of Electroanalytical Chemistry* **2002**, *519* (1–2), 93–100.

https://doi.org/10.1016/S0022-0728(01)00729-X.

(26) Kortlever, R.; Shen, J.; Schouten, K. J. P.; Calle-Vallejo, F.; Koper, M. T. M. Catalysts and Reaction Pathways for the Electrochemical Reduction of Carbon Dioxide. *Journal of Physical Chemistry Letters* **2015**, *6* (20), 4073–4082. https://doi.org/10.1021/acs.jpclett.5b01559.

(27) Ma, S.; Luo, R.; Moniri, S.; Lan, Y.; Kenis, P. J. a. Efficient Electrochemical Flow System with Improved Anode for the Conversion of CO2 to CO. *Journal of The Electrochemical Society* **2014**, *161* (10), F1124–F1131. https://doi.org/10.1149/2.1201410jes.

(28) Larrazábal, G. O.; Martín, A. J.; Pérez-Ramírez, J. Building Blocks for High Performance in Electrocatalytic CO 2 Reduction: Materials, Optimization Strategies, and Device Engineering. *The Journal of Physical Chemistry Letters* **2017**, *8* (16), 3933–3944. https://doi.org/10.1021/acs.jpclett.7b01380.

(29) Alvarez-Guerra, M.; Quintanilla, S.; Irabien, A. Conversion of Carbon Dioxide into Formate Using a Continuous Electrochemical Reduction Process in a Lead

Cathode. *Chemical Engineering Journal* **2012**, *207–208*, 278–284. https://doi.org/10.1016/j.cej.2012.06.099.

(30) Agarwal, A. S.; Zhai, Y.; Hill, D.; Sridhar, N. The Electrochemical Reduction of Carbon Dioxide to Formate/Formic Acid: Engineering and Economic Feasibility. *ChemSusChem* **2011**, *4* (9), 1301–1310. https://doi.org/10.1002/cssc.201100220.

(31) Chi, D.; Yang, H.; Du, Y.; Lv, T.; Sui, G.; Wang, H.; Lu, J. Morphology-Controlled CuO Nanoparticles for Electroreduction of CO 2 to Ethanol. *RSC Advances* **2014**, *4* (70), 37329–37332. https://doi.org/10.1039/c4ra05415f.

(32) Albo, J.; Sáez, A.; Solla-Gullón, J.; Montiel, V.; Irabien, A. Production of Methanol from CO2 Electroreduction at Cu2O and Cu2O/ZnO-Based Electrodes in Aqueous Solution. *Applied Catalysis B: Environmental* **2015**, *176–177* (MAY), 709–717. https://doi.org/10.1016/j.apcatb.2015.04.055.

(33) Albo, J.; Irabien, A. Cu2O-Loaded Gas Diffusion Electrodes for the Continuous Electrochemical Reduction of CO2 to Methanol. *Journal of Catalysis* **2016**, *343*, 232–239. https://doi.org/10.1016/j.jcat.2015.11.014.

(34)  Albo, J.; Beobide, G.; Castaño, P.; Irabien, A. Methanol Electrosynthesis from CO

2 at Cu 2 O/ZnO Prompted by Pyridine-Based Aqueous Solutions. *Journal of CO2*

*Utilization* **2017**, *18*, 164–172. https://doi.org/10.1016/j.jcou.2017.02.003.

(35)  Andrews, E.; Ren, M.; Wang, F.; Zhang, Z.; Sprunger, P.; Kurtz, R.; Flake, J.

Electrochemical Reduction of CO2 at Cu Nanocluster / (100) ZnO Electrodes.

*Journal of the Electrochemical Society* **2013**, *160* (11), H841–H846.

https://doi.org/10.1149/2.105311jes.

(36)  Albo, J.; Perfecto-Irigaray, M.; Beobide, G.; Irabien, A. Cu/Bi Metal-Organic

Framework-Based Systems for an Enhanced Electrochemical Transformation of

CO2 to Alcohols. *Journal of CO2 Utilization* **2019**, *33* (January), 157–165.

https://doi.org/10.1016/j.jcou.2019.05.025.

(37)  Albo, J.; Vallejo, D.; Beobide, G.; Castillo, O.; Castaño, P.; Irabien, A. Copper-

Based Metal-Organic Porous Materials for CO 2 Electrocatalytic Reduction to

Alcohols.        *ChemSusChem*        **2017**,        *10*        (6),        1100–1109.

https://doi.org/10.1002/cssc.201600693.

(38) Kotb, Y.; Fateen, S.-E. K.; Albo, J.; Ismail, I. Modeling of a Microfluidic Electrochemical Cell for the Electro-Reduction of CO 2 to CH 3 OH. *Journal of The Electrochemical Society* **2017**, *164* (13), E391–E400. https://doi.org/10.1149/2.0741713jes.

(39) Georgopoulou, C.; Jain, S.; Agarwal, A.; Rode, E.; Dimopoulos, G.; Sridhar, N.; Kakalis, N. On the Modelling of Multidisciplinary Electrochemical Systems with Application on the Electrochemical Conversion of CO2 to Formate/Formic Acid. *Computers & Chemical Engineering* **2016**, *93*, 160–170. https://doi.org/10.1016/j.compchemeng.2016.06.012.

(40) Merino-Garcia, I.; Albo, J.; Irabien, A. Tailoring Gas-Phase CO 2 Electroreduction Selectivity to Hydrocarbons at Cu Nanoparticles. *Nanotechnology* **2018**, *29* (1), 014001. https://doi.org/10.1088/1361-6528/aa994e.

(41) Zhang, B.; Ye, D.; Sui, P.-C.; Djilali, N.; Zhu, X. Computational Modeling of Air-Breathing Microfluidic Fuel Cells with Flow-over and Flow-through Anodes. *Journal of Power Sources* **2014**, *259*, 15–24.

https://doi.org/10.1016/j.jpowsour.2014.02.076.

(42) Zenyuk, I. V.; Das, P. K.; Weber, A. Z. Understanding Impacts of Catalyst-Layer

Thickness on Fuel-Cell Performance via Mathematical Modeling. *Journal of The*

*Electrochemical Society* **2016**, *163* (7), F691–F703.

https://doi.org/10.1149/2.1161607jes.

(43) Luo, G.; Ji, Y.; Wang, C.-Y.; Sinha, P. K. Modeling Liquid Water Transport in Gas

Diffusion Layers by Topologically Equivalent Pore Network. *Electrochimica Acta*

**2010**, *55* (19), 5332–5341. https://doi.org/10.1016/j.electacta.2010.04.078.

(44) El-Kharouf, A.; Mason, T. J.; Brett, D. J. L.; Pollet, B. G. Ex-Situ Characterisation

of Gas Diffusion Layers for Proton Exchange Membrane Fuel Cells. *Journal of*

*Power Sources* **2012**, *218*, 393–404.

https://doi.org/10.1016/j.jpowsour.2012.06.099.

(45) Shah, A. A.; Watt-Smith, M. J.; Walsh, F. C. A Dynamic Performance Model for

Redox-Flow Batteries Involving Soluble Species. *Electrochimica Acta* **2008**, *53*

(27), 8087–8100. https://doi.org/10.1016/j.electacta.2008.05.067.

(46) Fuller, E. N.; Schettler, P. D.; Giddings, J. C. NEW METHOD FOR PREDICTION OF BINARY GAS-PHASE DIFFUSION COEFFICIENTS. *Industrial & Engineering Chemistry* **1966**, *58* (5), 18–27. https://doi.org/10.1021/ie50677a007.

(47) Gupta, N.; Gattrell, M.; MacDougall, B. Calculation for the Cathode Surface Concentrations in the Electrochemical Reduction of CO2 in KHCO3 Solutions. *Journal of Applied Electrochemistry* **2006**, *36* (2), 161–172. https://doi.org/10.1007/s10800-005-9058-y.

(48) Newman, J.; Thomas-Alyea, K. E. *Electrochemical Systems*; The ECS Series of Texts and Monographs; Wiley, 2012.

(49) Cussler, E. L. *Diffusion: Mass Transfer in Fluid Systems*; Cambridge Series in Chemical Engineering; Cambridge University Press, 2009.

(50) P, D. *CRC Handbook of Chemistry and Physics*; CRC Press, 1992; Vol. 268. https://doi.org/10.1016/0022-2860(92)85083-s.

(51) Ubong, E. U.; Shi, Z.; Wang, X. Three-Dimensional Modeling and Experimental

Study of a High Temperature PBI-Based PEM Fuel Cell. *Journal of The Electrochemical Society* **2009**, *156* (10), B1276. https://doi.org/10.1149/1.3203309.

(52)  Yang, W. W.; Zhao, T. S. A Two-Dimensional, Two-Phase Mass Transport Model for Liquid-Feed DMFCs. *Electrochimica Acta* **2007**, *52* (20), 6125–6140. https://doi.org/10.1016/j.electacta.2007.03.069.

(53)  Knehr, K. W.; Kumbur, E. C. Open Circuit Voltage of Vanadium Redox Flow Batteries: Discrepancy between Models and Experiments. *Electrochemistry Communications* **2011**, *13* (4), 342–345. https://doi.org/10.1016/j.elecom.2011.01.020.

(54)  Ni, M. An Electrochemical Model for Syngas Production by Co-Electrolysis of H2O and CO2. *Journal of Power Sources* **2012**, *202*, 209–216. https://doi.org/10.1016/j.jpowsour.2011.11.080.

(55)  Kuhl, K. P.; Cave, E. R.; Abram, D. N.; Jaramillo, T. F. New Insights into the Electrochemical Reduction of Carbon Dioxide on Metallic Copper Surfaces. *Energy & Environmental Science* **2012**, *5* (5), 7050. https://doi.org/10.1039/c2ee21234j.

(56)   Verma, S.; Kim, B.; Jhong, H. R. M.; Ma, S.; Kenis, P. J. A. A Gross-Margin Model

for Defining Technoeconomic Benchmarks in the Electroreduction of CO2.

*ChemSusChem* **2016**, No. 3, 1972–1979. https://doi.org/10.1002/cssc.201600394.

(57)   Yoon, S. K.; Fichtl, G. W.; Kenis, P. J. A. Active Control of the Depletion Boundary

Layers in Microfluidic Electrochemical Reactors. *Lab on a Chip* **2006**, *6* (12), 1516–

1524. https://doi.org/10.1039/b609289f.

(58)   Del Castillo, A.; Alvarez-Guerra, M.; Irabien, A. Continuous Electroreduction of CO

2 to Formate Using Sn Gas Diffusion Electrodes. *AIChE Journal* **2014**, *60* (10),

3557–3564. https://doi.org/10.1002/aic.14544.

(59)   Lu, X.; Leung, D. Y. C.; Wang, H.; Xuan, J. A High Performance Dual Electrolyte

Microfluidic Reactor for the Utilization of CO 2. *Applied Energy* **2017**, *194*, 549–559.

https://doi.org/10.1016/j.apenergy.2016.05.091.

**For Table of Contents Use Only**

1
2
3
4
5
6
7
8
9
10
11
12
13
14
15
16
17
18
19
20
21
22
23
24
25
26
27
28
29
30
31
32
33
34
35
36
37
38
39
40
41
42
43
44
45
46
47
48
49
50
51
52
53
54
55
56
57
58
59
60